Original Article

MOLECULAR
METABOLISM

Sonic Hedgehog receptor Patched deficiency in astrocytes enhances glucose metabolism in mice

Linda Tirou [1], Mariagiovanna Russo [1], Helene Faure [1], Giuliana Pellegrino [1], Clement Demongin [1], Mathieu Daynac [1], Ariane Sharif [2], Jeremy Amosse [3,4], Soazig Le Lay [3,5], Raphaël Denis [6], Serge Luquet [6], Mohammed Taouis [7], Yacir Benomar [7], Martial Ruat [1,*]

ABSTRACT

Objective: Astrocytes are glial cells proposed as the main Sonic hedgehog (Shh)-responsive cells in the adult brain. Their roles in mediating Shh functions are still poorly understood. In the hypothalamus, astrocytes support neuronal circuits implicated in the regulation of energy metabolism. In this study, we investigated the impact of genetic activation of Shh signaling on hypothalamic astrocytes and characterized its effects on energy metabolism.

Methods: We analyzed the distribution of gene transcripts of the Shh pathway (*Ptc*, *Gli1*, *Gli2*, and *Gli3*) in astrocytes using single molecule fluorescence in situ hybridization combined with immunohistofluorescence of Shh peptides by Western blotting in the adult mouse hypothalamus. Based on the metabolic phenotype, we characterized Glast-Cre^{ERT2}-YFP-Ptc$^{-/-}$ (YFP-Ptc$^{-/-}$) mice and their controls over time and under a high-fat diet (HFD) to investigate the potential effects of conditional astrocytic deletion of the Shh receptor Patched (Ptc) on metabolic efficiency, insulin sensitivity, and systemic glucose metabolism. Molecular and biochemical assays were used to analyze the alteration of key pathways modulating energy metabolism, insulin sensitivity, glucose uptake, and inflammation. Primary astrocyte cultures were used to evaluate a potential role of Shh signaling in astrocytic glucose uptake.

Results: Shh peptides were the highest in the hypothalamic extracts of adult mice and a large population of hypothalamic astrocytes expressed *Ptc* and *Gli1-3* mRNAs. Characterization of Shh signaling after conditional Ptc deletion in the YFP-Ptc$^{-/-}$ mice revealed heterogeneity in hypothalamic astrocyte populations. Interestingly, activation of Shh signaling in Glast^{+} astrocytes enhanced insulin responsiveness as evidenced by glucose and insulin tolerance tests. This effect was maintained over time and associated with lower blood insulin levels and also observed under a HFD. The YFP-Ptc$^{-/-}$ mice exhibited a lean phenotype with the absence of body weight gain and a marked reduction of white and brown adipose tissues accompanied by increased whole-body fatty acid oxidation. In contrast, food intake, locomotor activity, and body temperature were not altered. At the cellular level, Ptc deletion did not affect glucose uptake in primary astrocyte cultures. In the hypothalamus, activation of the astrocytic Shh pathway was associated with the upregulation of transcripts coding for the insulin receptor and liver kinase B1 (LKB1) after 4 weeks and the glucose transporter GLUT-4 after 32 weeks.

Conclusions: Here, we define hypothalamic Shh action on astrocytes as a novel master regulator of energy metabolism. In the hypothalamus, astrocytic Shh signaling could be critically involved in preventing both aging- and obesity-related metabolic disorders.

Keywords Hypothalamus; Astrocyte; Glucose; Aging; Obesity; Hedgehog

1. INTRODUCTION

In the mature central nervous system (CNS), the Sonic hedgehog (Shh) signaling pathway is associated with stem cell maintenance in the main neurogenic niches and brain repair. Shh signaling also contributes to shaping neuronal and glial circuit plasticity and is involved in the communication between neurons and glial cells [1,2]. The astrocytes have been identified as the main cells that respond to Shh in the CNS [3]. Astrocytic Shh signaling observed after brain injury promotes neuroprotection [4], whereas activation of the pathway in these cells may be responsible for a decrease in neuronal activity [5,6] and regulating their functional properties [7]. Tumor-associated astrocytes secreting Shh also promote the growth of medulloblastoma [8]. The amino-terminal active fragment of Shh

[1]CNRS, Paris-Saclay University, UMR-9197, Neuroscience Paris-Saclay Institute, F-91198, Gif-sur-Yvette, France [2]Univ. Lille, Inserm, CHU Lille, U1172 - LilNCog (JPARC) - Lille Neurosciences & Cognition, F-59000, Lille, France [3]Univ. Angers SFR ICAT, F-49100, Angers, France [4]IRSET Laboratory, Inserm, UMR, 1085, Rennes, France [5]Univ. Nantes, CNRS, Inserm, Thorax Institut, F-44000, Nantes, France [6]Univ. Paris, BFA, UMR 8251, CNRS, F-75013, Paris, France [7]CNRS, Paris-Saclay University, UMR 9197, Neuroscience Paris-Saclay Institute, Molecular Neuroendocrinology of Food Intake, Orsay, France

*Corresponding author. CNRS, UMR-9197, Neuroscience Paris-Saclay Institute, 1 Avenue de la Terrasse, F-91198, Gif-sur-Yvette, France. E-mail: ruat@inaf.cnrs-gif.fr (M. Ruat).

Received November 16, 2020 • Revision received January 12, 2021 • Accepted January 21, 2021 • Available online 26 January 2021

https://doi.org/10.1016/j.molmet.2021.101172

(ShhN), which results from the cleavage of a Shh precursor, is widely distributed in the adult rodent brain. Shh is proposed to be secreted or axonally transported by various neuron populations, including GABAergic, cholinergic, and cerebrocortical neurons [1,2]. A subpopulation of mature oligodendroglial cells was recently described as a potential source of Shh protein [9]. In the brain, the Shh ligand and its associated signaling pathway have been proposed to be critical for palliating some physiological defects associated with neurodegenerative diseases such as Parkinson's disease [10] and remyelination by regulating adult-born progenitors to provide new oligodendrocytes [11,12].

Activation of Shh signaling requires the binding of the Shh ligand to its receptor Patched (Ptc). This binding will de-repress the constitutive inhibition exerted by Ptc on Smoothened (Smo), a G-protein-coupled receptor, and lead to a complex modulation of the zinc finger transcription factors glioma-associated oncogenes 1—3 (Gli1, Gli2, and Gli3). Activation of canonical Shh signaling leads to the upregulation of target genes including *Gli1* and *Ptc* [13,14]. However, several non-canonical mechanisms of Shh signaling independent of *Gli1* transcription increase and often depending on non-transcriptional events have been reported in neural tissues during development and adulthood [2,13]. Other non-canonical mechanisms of Shh signaling such as insulin-independent glucose uptake or anti-adipogenic effects that are AMP-activated protein kinase (AMPK)-dependent still have to be characterized in neural cells [15,16]. Of interest, one of the main roles of astrocytes is to provide metabolic support to brain cells. Hypothalamic astrocytes, through insulin signaling, are crucial for the control of glucose transport from the blood into the brain. Astrocytic insulin signaling is also critically involved in glucose-induced activation of hypothalamic pro-opiomelanocortin (POMC) neurons known to play a key role in the control of energy metabolism and glucose homeostasis [17—19]. In the hypothalamus, the expression of Shh and its receptor Ptc [20,21] as well as the transcription factors Gli1-Gli3 [3] have been reported in rats and mice, respectively. However, a detailed analysis of their distribution and the potential role of Shh signaling in the hypothalamic control of energy metabolism remains unknown.

Here, we combined in vitro and in vivo genetic activation of Shh signaling in hypothalamic astrocytes to study its potential roles in the control of energy homeostasis. We report for the first time that astrocytic Shh signaling is critically involved in the regulation of whole-body energy homeostasis. Interestingly, fasted mutant animals with Ptc-specific deletion in Glast (astrocyte-specific glutamate uptake transporter)$^+$ cells displayed enhanced insulin sensitivity, improved glucose tolerance, and decreased blood insulin levels. Mice lacking Ptc in Glast$^+$ cells also exhibited a lean phenotype over time characterized by a marked decrease in white (WAT) and brown (BAT) adipose tissues accompanied by an increase in fatty acid oxidation. Of interest, astrocytic Shh signaling enabled the counteraction of age-associated and diet-induced metabolic alterations. Ptc deletion did not affect glucose uptake in primary astrocyte cultures, suggesting that Ptc is not involved in astrocytic glucose uptake. Activation of the astrocytic Shh pathway increased the gene expression of the insulin receptor and liver kinase B1 (LKB1) after 4 weeks post-Ptc deletion and upregulated the mRNA levels of glucose transporter GLUT-4 after 32 weeks. Altogether, our data report an unsuspected novel role of Shh signaling in astrocytes for hypothalamic regulation of energy metabolism in the adult mouse brain.

2. MATERIALS AND METHODS

2.1. Animal procedures

C57BL6/J were purchased from Janvier Labs (France). Glast-Cre^{ERT2};Ptc$^{f/f}$;R26R—YFP (called YFP-Ptc$^{-/-}$ after recombination) and Ptc$^{f/f}$;R26R—YFP offspring were generated as previously described [22]. Adult male mice were used except when stated. The animals were group-housed, maintained in a 12-h light/12-h dark cycle with food and water ad libitum, and individually caged for metabolic experiments. To generate diet-induced obesity (DIO) mouse models, the YFP-Ptc$^{+/+}$ and YFP-Ptc$^{-/-}$ mice were placed on a high-fat diet (HFD; #U8978P) with 60% kcal from fat or a standard chow diet (CD; #M20) with 8% kcal from fat (Special Diet Services, France) for 12 weeks. The animals' body weights were measured regularly. Adult YFP-Ptc$^{+/+}$ and YFP-Ptc$^{-/-}$ mice were used for glucose and insulin-tolerance tests, hormone assays, and metabolic experiments. All the animal experiments were conducted in accordance with the Council Directive 2010/63EU of the European Parliament and approved (project no. 4558) by the French ethics committee (C2EA, 59 Comite Paris Centre et Sud).

2.2. Hypothalamic astrocyte primary culture and AAV infection

Hypothalami were dissected from post-natal day 1 (P1) pups from Ptc$^{f/f}$;R26R—YFP mice and maintained in cold DMEM/F-12 (#31330.038, Invitrogen). Tissues were crushed through a 20-μm Nylon mesh (Buisine, Clermont de l'Oise, France) using a cell scraper and cells centrifuged and seeded in T25 flasks in DMEM/F-12 supplemented with 10% heat-inactivated fetal calf serum (FCS) and 100 units/ml of penicillin-streptomycin both from Invitrogen. The cells were incubated at 37 °C under 5% CO$_2$ until confluency (12—15 days in vitro (DIV)) with the medium changed every 3 days. To remove contaminants, the sealed flask was shaken for 24 h at room temperature with one change of equilibrated culture medium. The next day, the cells were split for future use**.**

Astrocytes from Ptc$^{f/f}$;R26R—YFP mice (DIV 8—18) were seeded in poly-D-lysine (PDL)-coated (Sigma) 24-well plates at a density of 50,000 cells per well. The next day, they were infected with AAV-Cre (#7012) or AAV-GFP (#7006) (Vector Biolabs) MOI 50,000 in 250 μl of serum-free DMEM-F12 + 0.4% AdenoBOOST (#SB-P-AV-101-01, Sirion Biotech) for 6 h. The cells were washed twice in PBS and then cultured in regular medium for 5 days. The medium was changed to serum-free media for 24 h and [^{3}H]-2-deoxy-D-glucose uptake assays, RNA extraction, and immunocytochemistry were performed the next day.

2.3. Cell line culture and transfection

All the cell lines were cultured at 37 °C under 5% CO$_2$ in DMEM (#41966-029, Invitrogen) with 10% FCS. HEK293 and NIH3T3 cell lines were from ATCC and 4C20 Smo$^{-/-}$ and P2A6 Ptc$^{-/-}$ mouse embryonic fibroblast lines (MEFs) were kindly provided by Dr. P. Beachy (Stanford University School of Medicine, Stanford, CA, USA). HEK293 were transfected using X-tremeGENE9 (Sigma) with pRK5-mouse Shh (P. Beachy), pRK5-mouse Ptc, or pRK5 empty vector [23] and harvested 48 h later for western blotting analysis. The MEFs were seeded into PDL-coated 24-well plates at 50,000 cells/well and transfected using 0.75 μl of TransIT-2020 reagent (Mirus) and 10 ng of pRK5-mouse Ptc or pRK5-mouse Smo [23] supplemented with pRK5 empty vector (240 ng). The cells were starved 24 h later to perform [^{3}H]-2-deoxy-D-glucose uptake assays or RNA extraction 48 h post-transfection.

2.4. [^{3}H]-2-deoxy-D-glucose uptake assay

The assay was conducted on astrocytes or MEFs after 24 h of starvation. The plates were washed once with warm glucose-free DMEM (#11966025, Invitrogen) and incubated for 15 min in the same medium. The final 50 nM of 2-deoxy-D-glucose (2-DG) (Sigma) including 0.2 µci (12.3 nM) of [^{3}H]-2-deoxy-D-glucose (specific activity: 35.2 Ci/mmol, PerkinElmer) was added and incubated for 15 min. Reactions were terminated by aspiration and the wells washed four times with 500 µl of cold Krebs-HEPES buffer (113 mM of NaCl, 3 mM of KCl, 1.2 mM of KH_2PO_4, 1.2 mM of $MgSO_4$, 2.5 mM of $CaCl_2$, 25 mM of $NaHCO_3$, 5.5 mM of glucose, 1.5 mM of HEPES, and pH 7.2). Cells were digested (0.2 M of NaOH, 30 min, 50 °C, and 500 µl), the radioactivity was quantified using a liquid scintillation counter (Wallac), and the protein content was determined using Bradford protein assays (Sigma). Cytochalasin B (10 mM, Sigma) was used to determine the nonfacilitated [^{3}H]-2-deoxy-D-glucose uptake. The glucose uptake was assessed using three different astrocytes cultures and two independent experiments for MEFs.

2.5. Western blotting

Tissues from C57BL/6J adult mice ($n = 10$ for the SVZ, hypothalamus, and hippocampus; $n = 3$ for the cortex and cerebellum) were homogenized in 10 mM of ice-cold Tris–HCl buffer, pH 7.4, and 1 mM of EDTA supplemented with complete inhibitor cocktail (TE) (Sigma) and membranes were prepared by centrifugation at 100,000 g. Total homogenates of transfected HEK293 cells were prepared in TE. The protein content was determined using a Micro Lowry kit (Sigma). Proteins from the tissues (40 µg) and cell samples (3 µg) were electrophoresed and probed as previously described [24]. The following antibodies were used: goat anti-mSHH-N (N19, Santa Cruz, 1/2000), rabbit anti-mSHH-N (167Ab, 1/1000 [24]), and rabbit anti-tubulin (T5192, Sigma, 1/1000). 167Ab blocking experiments were conducted as previously described [24]. N19 antibody was blocked by overnight pre-incubation at 4 °C with human SHH-N N19 peptide (4 µg/ml) (Santa Cruz). Chemiluminescence (Pierce ECL+, Thermo Fisher Scientific) was acquired with a Chemidoc apparatus (Bio-Rad) and a densitometry analysis was performed using ImageLab software (Bio-Rad).

2.6. Food intake, locomotor activity, body temperature, and indirect calorimetry

Six YFP-Ptc$^{+/+}$ and YFP-Ptc$^{-/-}$ mice 13 weeks after tamoxifen treatment were monitored for 8 h for energy expenditure, oxygen consumption, carbon dioxide production, respiratory exchange rate (RER; VCO_2/VO_2), food intake, and locomotor activity using metabolic cages (Labmaster; TSE Systems, Bad Homburg, Germany). Their activity was recorded using an infrared light beam-based locomotion monitoring system (beam breaks/h). The mice were individually housed with free access to regular chow and acclimated to their chambers for 48 h before experimental measurements. The data analysis was carried out with Excel XP (Microsoft) using extracted raw values of VO_2, VCO_2 (in ml/h), and energy expenditure (kJ/h). Each value was expressed either per total body weight or whole lean tissue mass extracted from an EchoMRI analysis as previously described [25]. See the Supplementary Methods for further details. The rectal body temperature was measured in the morning with a thermometer probe (BIO-TK8851, rectal probe BIOBRET-3) lubricated with Vaseline (Cooper).

2.7. Glucose- and insulin-tolerance tests

Glucose-tolerance tests (GTTs) were performed as previously described [26]. Overnight fasted mice intraperitoneally received 2 g glucose/kg of body weight and blood samples were collected through their tail vein ($n = 4$–7/group). Plasma glucose was determined at 0, 15, 30, 60, and 120 min post-glucose challenge using an Accu-Check system. For insulin-tolerance tests (ITTs), the mice were fasted for 5 h and received an intraperitoneal injection of 1 U insulin/kg of body weight ($n = 5$–7/group). Glycemia was determined as for the GTTs.

2.8. Hormone assays

Blood samples of overnight fasted mice ($n = 4$–9/group) were collected from their aortas and treated with 1% 0.4 M K3-EDTA (for 1-month post-tamoxifen-treated mice) or 12 U/mL of heparin (for a HFD or 7-month post-tamoxifen-treated mice). Plasma was collected by centrifugation (13,000 g at 4 °C for 30 min) and stored at −80 °C. Hormone plasma levels were assessed using mouse ELISA kits from MERCK-Millipore for insulin (EZRMI-13K), leptin (EZML682K), and adiponectin (EZMADP-60K). Non-esterified fatty acids (NEFAs) were assayed using a WAKO kit (Sobodia).

2.9. RNA isolation, RT-qPCR, and RT-PCR assays

RNA was extracted from dissected tissues of individual mouse ($n = 4$/group) or MEFs (in two independent experiments with three biological replicates), reverse transcribed, and submitted to real-time quantitative PCR (qPCR) as previously described [26]. GAPDH and β-actin were used as internal controls. Specific qPCR primers (Eurofins) are listed in Supplemental Table 2. For conventional RT-PCR of Ptc transcripts from mouse tissues and MEFs, cDNAs were prepared as previously described for qPCR. They were then amplified using Flexi Go-Taq (Promega) with primers (mPTC11; 5′-AAAGCCGAAGTTGGCCATGGGTAC-3′ and mPTC7R; and 5′-TGTCCTGTTTCACTGAATGC-3′) previously described [27].

2.10. Immunohistochemistry

Mice under deep anesthesia were perfused with 4% paraformaldehyde (PFA). Brain sections were cut on a cryostat (14 µm) ($n = 3$–4/group). For immunostaining, the sections were incubated for 1 h in PBS, 0.25% Triton-X100, and 1% BSA and 1 h with donkey anti-mouse Fab fragment (1/50, 715-007-003, Jackson IR). The primary antibodies were incubated overnight at 4 °C: chicken anti-GFP (1/1000, GFP-1020, Avès Labs) for YFP detection, rabbit anti-GFAP (1/500, Z033429-2, Dako), mouse anti-S100β (1/500, S2532, Sigma), mouse anti-HuC/D (1/500, A21271, Molecular Probes), and rabbit anti-NG2 (1/400, AB5320, Millipore). The slices were then incubated with the appropriate fluorescent secondary antibody (1/400, Millipore or Jackson IR) for 2 h at room temperature. Staining was replicated on at least three different mice as indicated. Nuclei were counterstained with DAPI. Images were acquired with a 20X objective (N.A. 0.75) using a fluorescence microscope (Leica DM2000) or a 63X objective on a confocal microscope (Leica TCS SP8). For the latter, Z stacks 5.9 µm thick containing 15 Z section images were analyzed using LAS-X software (Leica) and reconstructed in ImageJ 1.52p (NIH) and Photoshop CS3 (Adobe).

Small pieces of adipose tissues were fixed for 12–16 h at room temperature with 4% PFA at room temperature, embedded in paraffin, serially sectioned at 5 µm, stained with hematoxylin and eosin (HE), and evaluated using an Olympus AX60 conventional light microscope. Images of fat tissue areas were captured with a QIClick Color light camera (QI Imaging) using QCapture Pro software.

2.11. Immunocytochemistry

Cells on coverslips were washed twice in PBS, fixed for 20 min with ice-cold 4% PFA, and washed three times in PBS. Immunofluorescence was

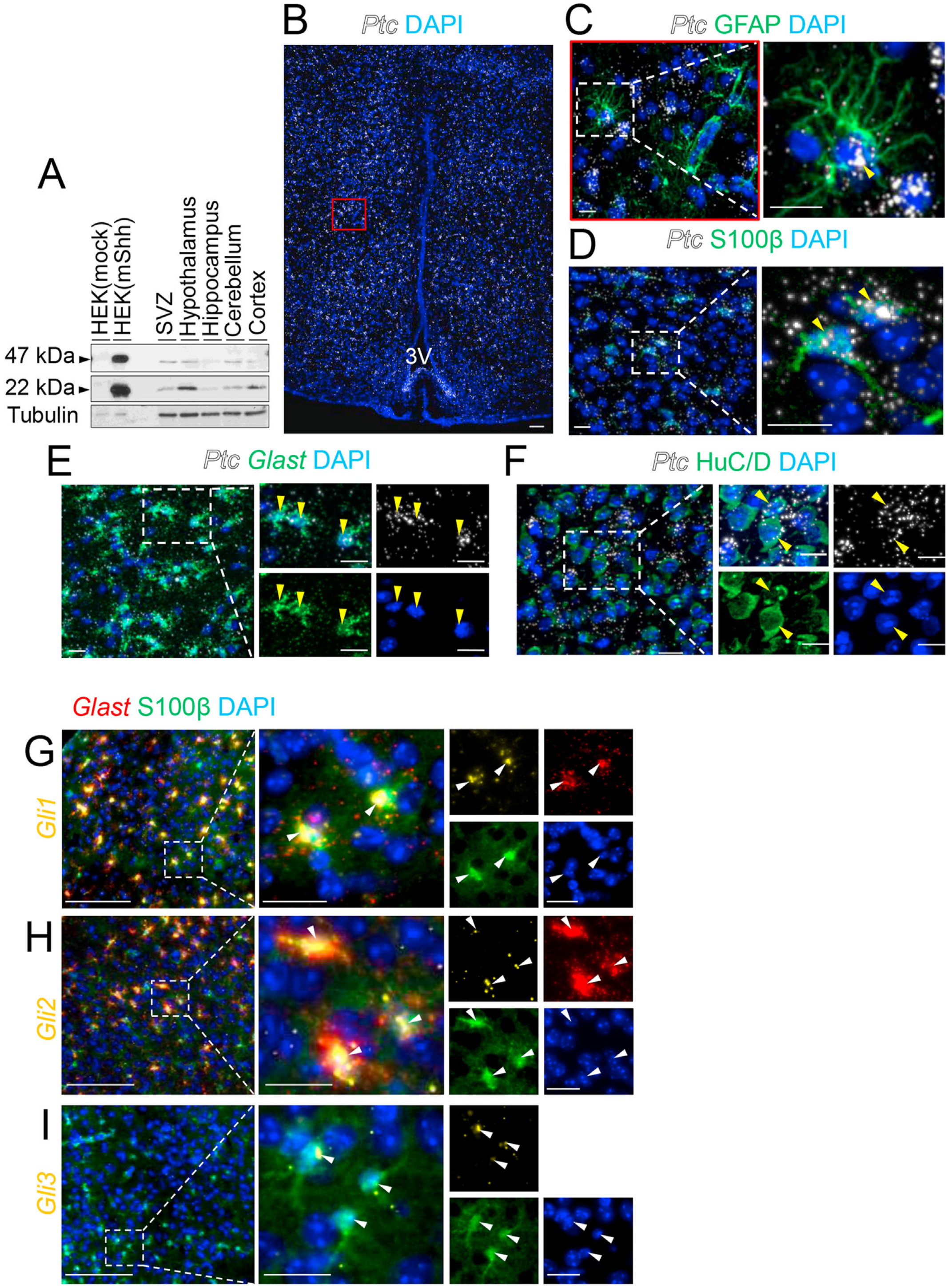

Figure 1: Analysis of hedgehog signaling in the mouse hypothalamus. (A) Western blotting analysis of hedgehog (Hh) protein levels in brain tissues from adult mice ($n = 3$) and HEK293 cells transfected with a mouse Sonic hedgehog (HEK (mShh)) or control (HEK (mock)) vector. N19 and 167Ab Shh antibodies revealed bands at 47 kDa and 22 kDa corresponding to Shh protein precursor and active forms, respectively. Tubulin served as a loading control (SVZ, subventricular zone of the lateral ventricles). (B–F) RNAscope of Patched (Ptc) mRNA combined with immunohistofluorescence for GFAP (C), S100β (D), HuC/D (F), or RNAscope for Glast mRNA (E) on coronal sections of the tuberal region of the hypothalamus from adult mice. Higher magnifications show Ptc mRNA (yellow arrowheads) in GFAP$^+$ (C), S100β$^+$ (D), Glast$^+$ (E), and HuC/D$^+$ (F) cells in the hypothalamic parenchyma and presented in merged and single channels with the nuclear marker DAPI. (G–I) RNAscope for Gli1 (G), Gli2 (H), and Gli3 (I) mRNAs combined with RNAscope for Glast mRNA (G and H) and immunohistofluorescence for S100β (G–I) on coronal sections of the tuberal region of the hypothalamus showing the ventromedial hypothalamic nuclei from the adult mice. Magnifications showing expression of Gli1, Gli2, and Gli3 mRNAs in *Glast*$^+$ S100β$^+$ cells (G and H) and S100β$^+$ cells (I) (white arrowheads), respectively, presented in merged and single channels with the nuclear marker DAPI. Staining was replicated on three mice. Scale bars, 100 μm in (B) and 20 μm in (C–I). 3V, third ventricle.

performed as previously described with 2 h of incubation in primary antibody (chicken anti-GFP; 1/300) and without Fab fragment blocking.

2.12. Single molecule fluorescent in situ hybridization

Single molecule fluorescent in situ hybridization (smfISH) was performed on 14 μm of frozen brain sections of adult mice ($n = 3$/group) using an RNAscope Multiplex Fluorescent kit v2 according to the manufacturer's protocols (Advanced Cell Diagnostics). The intensity was compared with identical parameters. Specific probes were used to detect Patched (Ptc): 402811-C2, Glast: 430781-C3, Gli1: 311001-C2, Gli2: 405771-C2, Gli3: 445511-C3, and Ptc^{del}: 581621 (floxed region of Ptc) mRNAs. Positive cells were associated with more than two RNAscope signals.

2.13. Statistics

Data are represented as mean ± standard error of the mean (SEM). Statistical significance was determined by unpaired two-tailed Student's t test (Excel) or the Mann–Whitney test (Anastats).

2.14. Cell counting and statistical analysis

Quantification of *Ptc*$^{del+}$*Glast*$^{+}$S100β^{+} co-staining in the hypothalamic parenchyma was performed on sections obtained at the level of the median eminence from three YFP-Ptc$^{+/+}$ and YFP-Ptc$^{-/-}$ mice 10 days after tamoxifen treatment. The number of *Glast*$^{+}$S100β^{+} cells per animal ranged between 28 and 48 in the arcuate nucleus (ARC) and 90 and 144 in the ventromedial hypothalamic nucleus (VMH).

Quantification of *Gli1*$^{+}$*Glast*$^{+}$S100β^{+}, *Gli2*$^{+}$*Glast*$^{+}$S100β^{+}, and *Gli3*$^{+}$S100β^{+} co-staining in the cerebral cortex and hypothalamic parenchyma was performed on sections obtained at the level of the median eminence from three YFP-Ptc$^{+/+}$ and YFP-Ptc$^{-/-}$ mice 10 days after tamoxifen treatment (except for *Gli2*$^{+}$*Glast*$^{+}$S100β^{+} in the arcuate of the YFP-Ptc$^{+/+}$ mice, $n = 2$). The number of *Glast*$^{+}$S100β^{+} cells per animal ranged between 34 and 67 in the ARC, 118 and 279 in the VMH, 133 and 332 in the dorsomedial hypothalamic nucleus (DMH), and 255 and 388 in the cerebral cortex. The number of S100β^{+} cells per animal ranged between 32 and 84 in the ARC, 141 and 216 in the VMH, 159 and 275 in the DMH, and 245 and 291 in the cerebral cortex. Counting the co-localized staining was done using the ROI and multipoint ImageJ tools. Quantitative data are expressed as the mean ± standard error of the mean (SEM). The two experimental groups were compared using the Mann–Whitney test. A value of $p < 0.05$ was considered statistically significant. Graphs were drawn using GraphPad Prism 5.2 (GraphPad Software, Inc).

3. RESULTS

3.1. Hypothalamic astrocytes expressed Patched and Gli1-3 transcription factors

We first investigated the expression of Sonic hedgehog (Shh) proteins in adult mouse brain tissues and HEK293 cells expressing mouse Shh using N19 and 167Ab, two specific Shh antibodies [24,28–30]. Using Western blotting, two bands of 47 kDa and 22 kDa corresponding to the uncleaved and aminoterminal active fragments of Shh (ShhN), respectively, were identified (Figure 1A). These signals were absent in blocking experiments (Figure Sup. 1A–D), consistent with the presence of uncleaved Shh and ShhN signals in these tissues. The hypothalamic extracts exhibited the highest expression levels of ShhN, suggesting elevated Shh signaling in this brain region.

To investigate Shh signaling in the hypothalamus, we used single molecule fluorescent in situ hybridization (smfISH), a highly sensitive technique, to determine the hypothalamic distribution of mRNAs encoding the Shh receptor Patched (Ptc) and Gli1-3 transcription factors associated with the pathway [1]. Using RNAscope, we successfully detected a wide distribution of Ptc mRNAs in adult hypothalamic nuclei, including the dorsomedial hypothalamic nucleus (DMH), ventromedial hypothalamic (VMH), and arcuate (ARC) nuclei (Figure 1B–F). We observed intense signals associated with Ptc mRNAs around the nuclei of *Glast*, GFAP, and S100β-positive cells in the various hypothalamic nuclei (Figure 1C–E). *Ptc*$^{+}$GFAP^{+} cells displayed a stellated morphology, suggesting that they were astrocytes (Figure 1C). Ptc mRNA expression was moderate in HuC/D^{+} cells corresponding to neurons in the hypothalamic parenchyma (Figure 1F). Interestingly, we further identified by RNAscope intense signals indicating the expression of *Gli1* and *Gli2* in *Glast*$^{+}$S100β^{+} cells (Figure 1G–H) and the moderate expression of *Gli3* in S100β^{+} cells (Figure 1I). Gli1-, Gli2-, and Gli3-associated RNAscope signals were rarely observed outside of these cells in the hypothalamus. Altogether, these data suggest that a large population of hypothalamic astrocytes express Ptc and Gli1-3 mRNAs and thus should be responsive to Shh signaling.

3.2. Deletion of the Shh receptor Ptc from *Glast*$^{+}$ astrocytes in adult mice

To investigate the role of Ptc in astrocytes, we used YFP-Ptc$^{+/+}$ and YFP-Ptc$^{-/-}$ mice [22,31] in which the YFP expression and Ptc deletion were initiated by tamoxifen (Tx)-mediated activation of the Cre recombinase in all of the progeny of the recombined glutamate aspartate transporter (Glast)-positive cells. We previously showed that recombination occurs in neural stem cells (NSCs) in the ventricular-subventricular zone (V-SVZ) of the lateral ventricles and astrocytes adjacent to this region upon Tx treatment in adult mice [22]. In the VMH of the YFP-Ptc$^{+/+}$ and YFP-Ptc$^{-/-}$ mice 7 days after Tx, we observed numerous YFP^{+} cells displaying a stellate morphology attributed to astrocytes. These cells were positive for the astroglial markers GFAP and S100β (Figure Sup. 2A–B and Figure Sup. 3A–H) but were not labeled by the neuronal marker HuC/D or oligodendrocyte precursor cell marker NG2 (Figure Sup. 2A–B and Figure Sup. 3I–L). These data showed that after Tx, YFP recombination occurred in GFAP and S100β-positive astrocytes in hypothalamic nuclei, consistent with the Glast-specific expression of Cre-recombinase.

To further characterize Ptc deletion upon Tx treatment, we analyzed the hypothalamic expression of transcripts for *Ptc* and *Ptc* deleted (*Ptc*^{del}) for the floxed region containing exons 8–9, which should have been removed in the YFP-Ptc$^{-/-}$ mice (Figure Sup. 2C–D). First, using RT-PCR, we detected Ptc^{del} mRNA only in the hypothalamus of the YFP-Ptc$^{-/-}$ mice 10 days after Tx while Ptc mRNA was detected in the YFP-Ptc$^{+/+}$ mice and was strongly decreased in the YFP-Ptc$^{-/-}$ mice (Figure Sup. 2C). Second, we assayed the expression of Ptc transcripts by RNAscope using a specific probe (Ptc^{del}) designed against the Ptc mRNA sequence, which should have been deleted in Glast^{+} recombined cells in the YFP-Ptc$^{-/-}$ mice (Figure Sup. 2D). We performed RNAscope for Ptc^{del} and Glast mRNAs combined with immunohistofluorescence (IHF) for the astrocyte marker S100β. Thus, we identified the Ptc mRNA expression in the vast majority (87–94%) of Glast^{+}S100β^{+} astrocytes in the hypothalamic parenchyma of the YFP-Ptc$^{+/+}$ mice 10 days after Tx as shown in the ARC and VMH nuclei (Figure Sup. 2E–I and Supplemental Table 1). In the YFP-Ptc$^{-/-}$ mice, Ptc mRNA signals were detected in only 12–14% of Glast^{+}S100β^{+} cells in the hypothalamic nuclei (Figure Sup. 2E–I and Supplemental Table 1). As a control for the Ptc^{del} probe, Ptc mRNAs were still observed in Glast/S100β-negative cells in the YFP-Ptc$^{-/-}$ mice

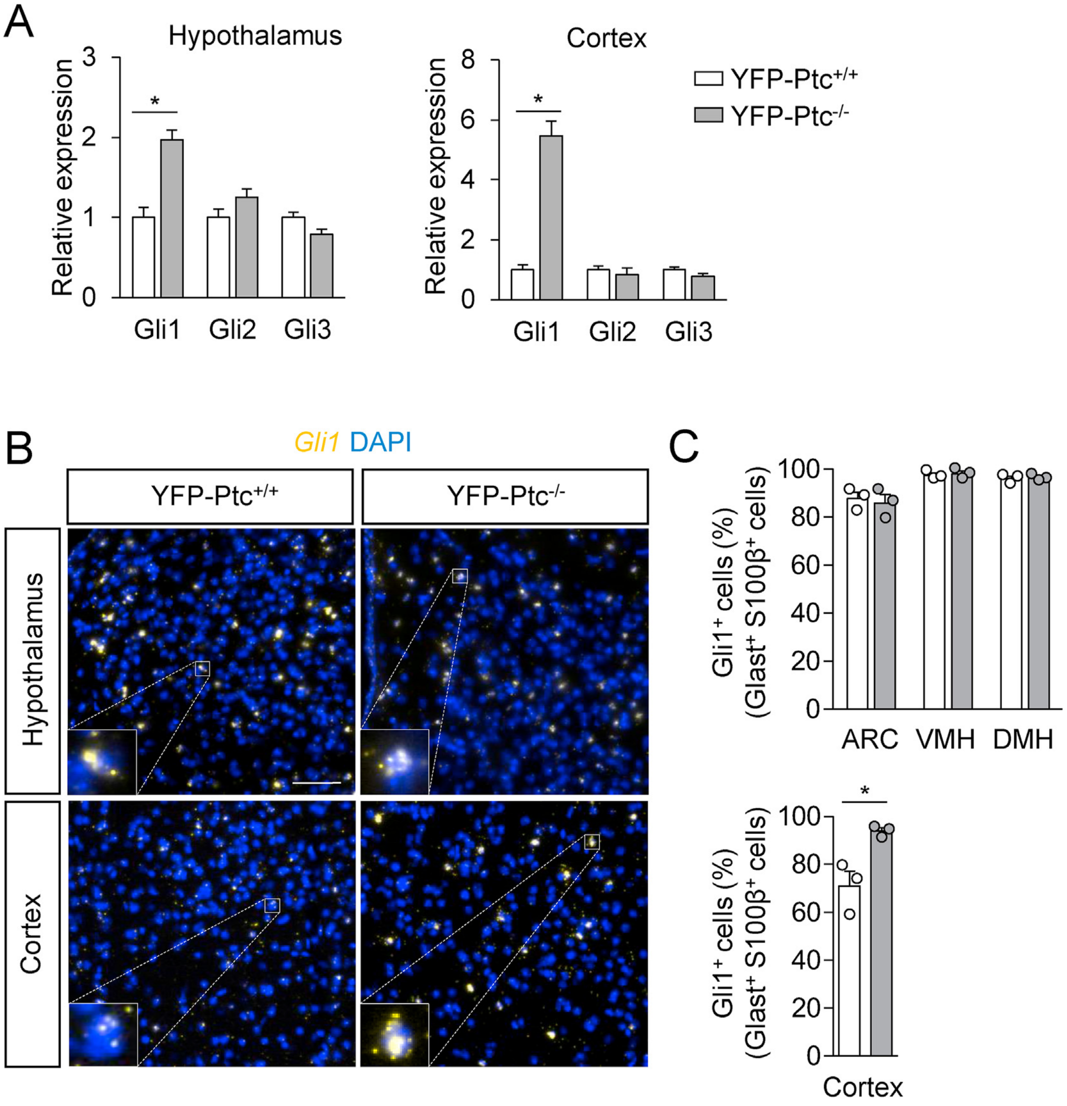

Figure 2: Analysis of hedgehog signaling in Glast$^+$ astrocytes after Patched deletion. (A) mRNA levels of *Gli1*, *Gli2*, and *Gli3* measured by qRT-PCR in the hypothalamus and cerebral cortex of the YFP-Ptc$^{+/+}$ and YFP-Ptc$^{-/-}$ mice 4 weeks after tamoxifen (Tx). Actin served as a housekeeping gene for relative mRNA expression levels (n = 4 mice). (B) RNAscope for *Gli1* and counterstaining for DAPI on coronal sections of the tuberal region of the hypothalamus highlighting the ventromedial hypothalamic nuclei and cerebral cortex of the YFP-Ptc$^{+/+}$ and YFP-Ptc$^{-/-}$ mice 10 days after Tx. Insets highlight the difference in RNAscope signal intensity between the hypothalamus and cerebral cortex at the level of a single cell. (C) Quantitative analysis of RNAscope signals for Gli1 mRNA in *Glast*$^+$ and S100β$^+$ cells in hypothalamic nuclei and cerebral cortex from the YFP-Ptc$^{+/+}$ and YFP-Ptc$^{-/-}$ mice. Bar graphs (A and C) represent mean ± SEM. n = 3–4 mice/group, $^*p < 0.05$ by the Mann–Whitney test. Staining was replicated on three mice. Scale bars, 50 μm in (B). ARC, arcuate nucleus; VMH, ventromedial hypothalamic nucleus; DMH, dorsomedial hypothalamic nucleus.

(Figure Sup. 2F and H, white arrowhead) as observed in the YFP-Ptc$^{+/+}$ mice (Figure Sup. 2G, white arrowhead) and with another Ptc RNAscope probe (Figure 1F). Further analysis of these data indicated that Ptc was deleted in 84–87% of triple Ptc$^+$Glast$^+$S100β$^+$ cells. Altogether, these results demonstrated Glast specificity and high efficiency of inducible Cre-mediated recombination upon Tx in the YFP-Ptc$^{+/+}$ and YFP-Ptc$^{-/-}$ mice, leading to Ptc deletion in Glast$^+$S100β$^+$ astrocytes in the YFP-Ptc$^{-/-}$ mice.

3.3. Ptc deficiency in Glast$^+$ astrocytes modified *Gli1* and *Gli3* transcription

We then explored whether the mRNA levels of Gli1, Gli2, and Gli3 transcription factors were modified in hypothalamic nuclei upon Ptc deficiency in Glast$^+$ astrocytes. In comparison, we analyzed the Gli1-3 distribution in the cerebral cortex, a region showing a low Shh protein expression (Figure 1A and Figure Sup. 1). In these brain regions, 4 weeks after Tx, Ptc deficiency in Glast$^+$ astrocytes induced a 2–6 fold increase in *Gli1* expression detected by qRT-PCR, whereas Gli2 and Gli3 mRNA levels were not modified (Figure 2A) as other genes associated with the Shh pathway (Figure Sup. 5C).

We then used RNAscope combined with IHF to investigate the expression of Gli1-2 and Gli3 mRNAs in *Glast*$^+$S100β$^+$ and S100β$^+$ astrocytes, respectively (Figure 2B–C and Figure Sup. 4A–L[4] and Figure Sup. 5A and B). Quantification of these experiments is described in Supplemental Table 1. These data indicated that 1) *Gli1* transcription was high in hypothalamic astrocytes and low in cerebrocortical astrocytes in the YFP-Ptc$^{+/+}$ mice (Figure 2B and Figure Sup. 4A–C[4] and G–I[4]); 2) the number of cortical astrocytes expressing *Gli1* increased

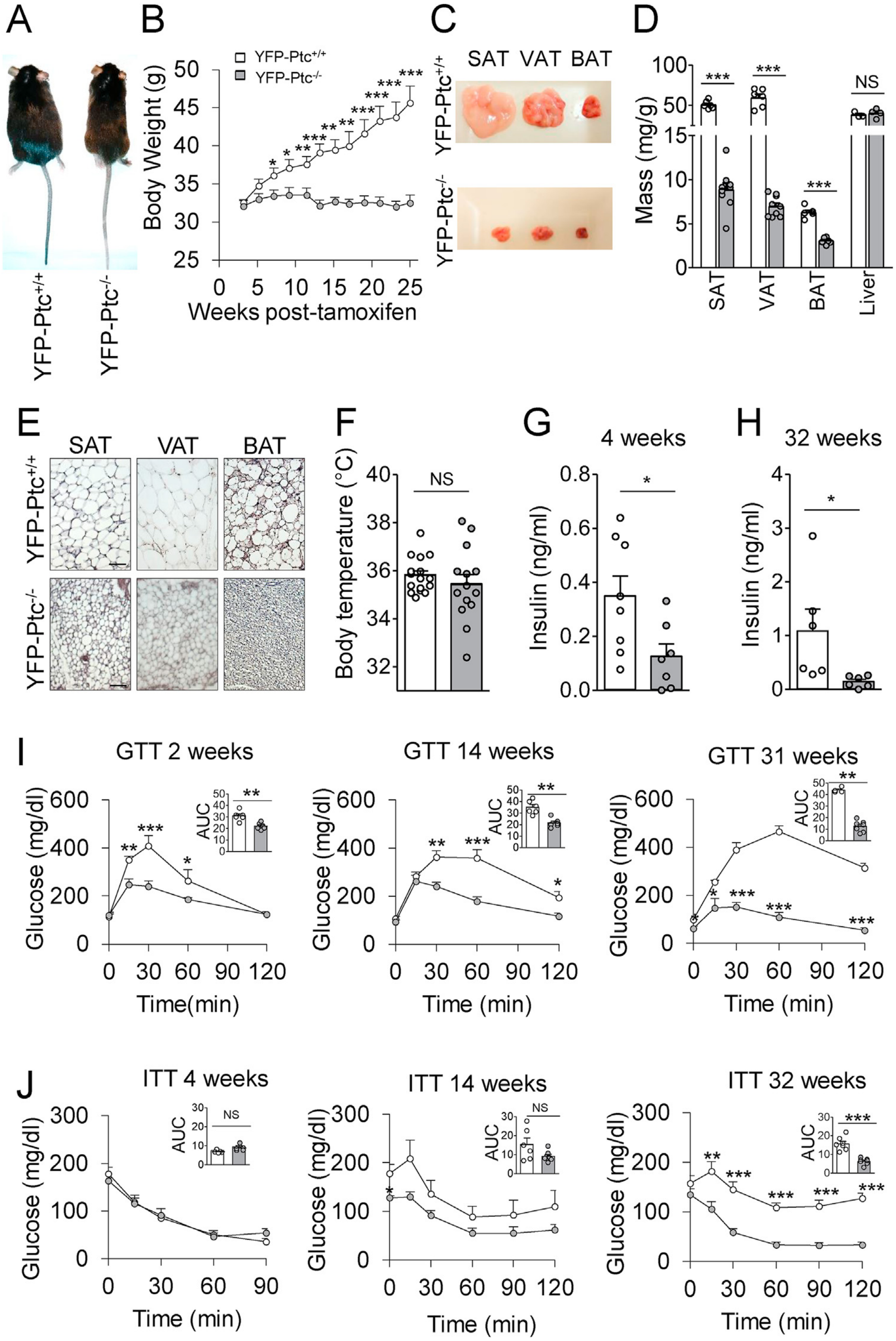

Figure 3: Deletion of Patched in Glast$^+$ astrocytes prevented age-associated metabolic alterations. (A) Representative images of the YFP-Ptc$^{+/+}$ and YFP-Ptc$^{-/-}$ mice 20 weeks after tamoxifen (Tx) treatment. (B) Time course of body weight. Data are represented as mean ± SEM, n = 7–10 mice/group. (C) Dissected subcutaneous (SAT), visceral (VAT), and brown (BAT) adipose tissues from the YFP-Ptc$^{+/+}$ and YFP-Ptc$^{-/-}$ mice 32 weeks after Tx. (D) Ratio of total organ to body weights. Masses of SAT, VAT, and BAT were reduced in the YFP-Ptc$^{-/-}$ mice, whereas liver mass did not differ between the two cohorts of mice. Data are represented as mean ± SEM. n = 6–9 mice/group for SAT, VAT, and BAT, n = 3–4 mice/group for the liver. (E) Representative hematoxylin and eosin (H&E)-stained sections of SAT, VAT, and BAT. Histology analysis of white and brown adipose tissues showed a strong reduction in cell size in SAT, VAT, and BAT in the YFP-Ptc$^{-/-}$ mice compared to their control animals. H&E staining was replicated on four mice per group. Scale bars, 100 μm. (F) Rectal temperature of the YFP-Ptc$^{+/+}$ (35.8 ± 0.2 °C) and YFP-Ptc$^{-/-}$ (35.5 ± 0.4 °C) mice was not different 25 weeks after Tx. Bar graphs represent mean ± SEM. n = 14–16 mice/group. (G–H) Plasma insulin levels of the overnight fasted YFP-Ptc$^{+/+}$ and YFP-Ptc$^{-/-}$ mice 4 (G) and 32 weeks (H) after Tx. Bar graphs represent mean ± SEM. n = 6–8 mice/group. (I–J) Evolution over time of glucose (I) and insulin (J) responses assessed by glucose- and insulin-tolerance tests performed on the fasted YFP-Ptc$^{+/+}$ and YFP-Ptc$^{-/-}$ mice. Weeks after Tx are indicated. Insets represent the area under the curve (AUC) of the associated graphs. Data are represented as mean ± SEM. n = 4–7 mice/group. *$p < 0.05$, **$p < 0.01$, and ***$p < 0.001$; NS, no significant change by Student's t test. GTT, glucose-tolerance test; ITT, insulin-tolerance test.

upon Ptc deficiency (Figure 2B–C and Figure Sup. 4G–L[4]); 3) the number of S100β^{+} astrocytes expressing *Gli3* significantly increased in the ARC and DMH but not in the VMH and decreased in the cerebral cortex of the YFP-Ptc$^{-/-}$ mice (Figure Sup. 5B); and 4) the number of Gli2-positive astrocytes was not affected by Ptc deletion (Figure Sup. 5A).

3.4. Ptc deficiency in Glast^{+} astrocytes reduced adiposity

We then assessed the phenotype of the YFP-Ptc$^{-/-}$ adult animals. These mice were born healthy and at a Mendelian ratio. However, 6 weeks after Tx, we observed that the YFP-Ptc$^{-/-}$ mice started to display a lean phenotype and were not gaining weight over time (Figure 3A–B). Further analysis revealed that subcutaneous (SAT), visceral (VAT), and brown (BAT) adipose tissues were severely affected in the YFP-Ptc$^{-/-}$ mice 32 weeks after Tx (Figure 3C). We performed histological and tissue weight analyses to quantify these defects. In the YFP-Ptc$^{-/-}$ mice, the adipocyte size was dramatically reduced and correlated with a decrease in total SAT (82%), VAT (88%), and BAT (52%) (Figure 3D–E). We did not detect any modification of tissue weight in the liver (Figure 3D). Despite a marked reduction in BAT, we did not observe any modification in the body temperature 25 weeks after Tx (Figure 3F).

3.5. Ptc deficiency in Glast^{+} astrocytes enhanced insulin sensitivity and glucose tolerance and increased fatty acid oxidation

Analysis of blood insulin in overnight fasted animals revealed a significant decrease in plasma insulin levels in the YFP-Ptc$^{-/-}$ animals compared to the YFP-Ptc$^{+/+}$ mice over time (Figure 3G–H). However, the blood insulin level was similar in the YFP-Ptc$^{-/-}$ mice 4 and 32 weeks after Tx, whereas it increased in the YFP-Ptc$^{+/+}$ mice 32 weeks after Tx (Table 1).

To further investigate the effects of Ptc deletion on glucose metabolism, we analyzed glucose and insulin tolerance, energy expenditure, and levels of key adipokines involved in glucose and lipid metabolism. Interestingly, glucose-tolerance tests (GTTs) revealed that the YFP-Ptc$^{-/-}$ mice displayed improved glucose tolerance that was maintained over time (Figure 3I). No difference during GTTs was detected between the two cohorts of mice before Tx (Figure Sup. 6A), demonstrating that Tx-induced Ptc deletion in Glast^{+} cells was responsible for the improved glucose tolerance in the YFP-Ptc$^{-/-}$ mice. GTTs performed two weeks after Tx revealed lower blood glucose concentrations after glucose injection in the YFP-Ptc$^{-/-}$ animals compared to the YFP-Ptc$^{+/+}$ mice, whereas it was in the same range between the two groups before and 120 min after glucose loads (Figure 3I). Consistent with this observation, the YFP-Ptc$^{+/+}$ mice exhibited a much higher area under the glucose tolerance curve (AUC) (Figure 3I). The adult female YFP-Ptc$^{-/-}$ mice also displayed improved glucose tolerance after Tx over time as evidenced by lower AUC (Figure Sup. 6B). Interestingly, 32 weeks after Tx, the YFP-Ptc$^{+/+}$ mice exhibited a marked glucose intolerance and did not return to the glucose baseline level (Figure 3I), presumably reflecting age-associated insulin resistance.

We then assessed whether Ptc deletion in astrocytes could affect whole-body insulin sensitivity. Insulin-tolerance tests (ITTs) performed during the first (4 and 14) weeks after Tx treatment revealed that the YFP-Ptc$^{-/-}$ mice did not exhibit altered insulin sensitivity compared to the YFP-Ptc$^{+/+}$ control mice (Figure 3J and Table 1). In contrast, 32 weeks after Tx treatment, blood glucose levels during ITTs were lower in the YFP-Ptc$^{-/-}$ mice than in the YFP-Ptc$^{+/+}$ mice. Accordingly, the area under the insulin-tolerance curve was markedly reduced (Figure 3J), presumably reflecting age-associated insulin resistance in the YFP-Ptc$^{+/+}$ mice, which was supported by high glucose levels observed in the GTTs of these animals (Figure 3I). Collectively, these data indicate that genetic activation of Shh signaling in Glast^{+} astrocytes enhances insulin sensitivity and improves glucose tolerance, preventing age-associated metabolic alterations.

Blood leptin was not modified 4 weeks after Tx between the YFP-Ptc$^{+/+}$ and YFP-Ptc$^{-/-}$ animals, increased in the YFP-Ptc$^{+/+}$ aged animals, but remained at a low level in the YFP-Ptc$^{-/-}$ mice 32 weeks after Tx (Table 1). This agreed with the reduced adipose tissue masses in the YFP-Ptc$^{-/-}$ animals (Figure 3C–E). Analysis of non-esterified fatty acid (NEFA) indicated a significantly lower concentration in the YFP-Ptc$^{-/-}$ animals 32 weeks after Tx, whereas no significant change occurred between the control and YFP-Ptc$^{-/-}$ mice 4 weeks after Tx. Interestingly, plasma adiponectin levels were similar in both groups (Table 1) despite the marked difference in the weight of white adipose tissues in these animals (Figure 3C–E), suggesting increased adiponectin production from the adipose tissue in the YFP-Ptc$^{-/-}$ mice.

No difference in food intake, energy expenditure, and locomotor activity was detected between the YFP-Ptc$^{-/-}$ and control mice 13 weeks after Tx treatment (Figure 4A–C). However, we reported an altered O$_2$ consumption/CO$_2$ production rate with a significant decrease in the respiratory exchange ratio, which was diminished during the day in the YFP-Ptc$^{-/-}$ mice (Figure 4D–E). These observations indicated that the percentage of fatty acid oxidation was significantly increased during the day in the YFP-Ptc$^{-/-}$ mice, whereas it was reduced at night (Figure 4F–G). Altogether, these data suggest that the YFP-Ptc$^{-/-}$ mice utilized fatty acid bulk energy during the day and transformed glucose to fatty acids at night, which should favor lipid-substrate catabolism.

Table 1 – Plasma variables in YFP-Ptc$^{+/+}$ and YFP-Ptc$^{-/-}$ fasted mice and high fat diet.

	YFP-Ptc$^{+/+}$	YFP-Ptc$^{-/-}$	YFP-Ptc$^{+/+}$	YFP-Ptc$^{-/-}$	YFP-Ptc$^{+/+}$	YFP-Ptc$^{-/-}$
	Chow diet				High fat diet$^{\Delta}$	
	4 weeks post–Tx		32 weeks post–Tx		22 weeks post–Tx	
Glucose (mg/dl)	97.8 ± 5.8	90.8 ± 7.5	99.0 ± 8.7	63.0 ± 7.5[a]	ND	ND
Insulin (ng/ml)	0.35 ± 0.08	0.13 ± 0.05[a]	1.09 ± 0.41	0.15 ± 0.04[a]	2.08 ± 0.24	0.15 ± 0.05[c]
Leptin (ng/ml)	0.31 ± 0.08	0.19 ± 0.04	14.8 ± 3.4	0.36 ± 0.21[b]	28.2 ± 4.9	2.4 ± 1.5[c]
NEFA (μmol/l)	1590 ± 83	1529 ± 91	1901 ± 180	1294 ± 78[a]	ND	ND
Adiponectin (ng/ml)	ND	ND	10822 ± 1230	12835 ± 1129	8457 ± 1061	10961 ± 881

Data are means ± SEM, n = 4–9/group.

[a] $p < 0.05$.

[b] $p < 0.01$.

[c] $p < 0.001$ vs age-matched YFP-Ptc+/+ mice by Student's t-test. $^{\Delta}$12 weeks of high fat diet. ND, not determined.

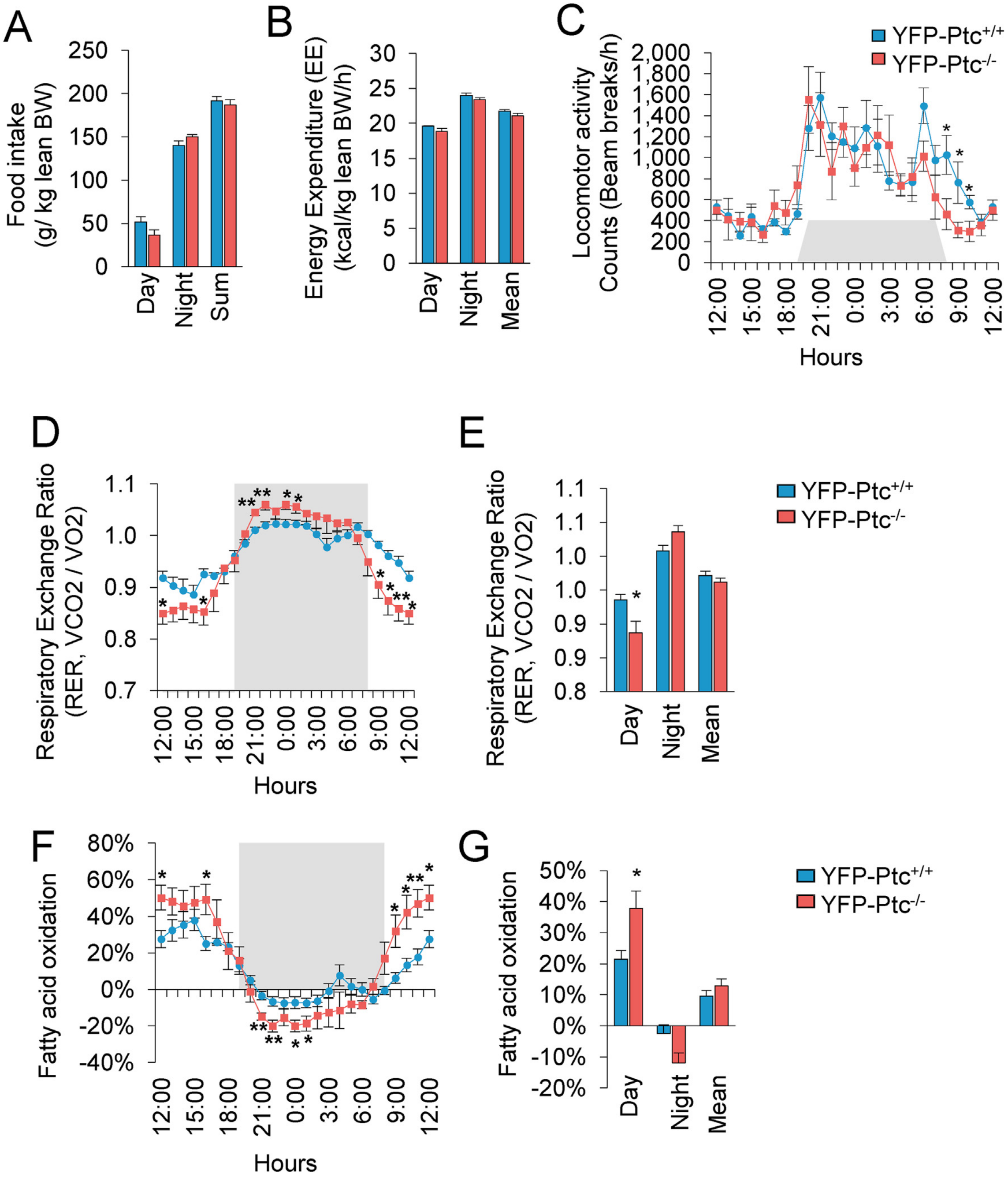

Figure 4: Mice deleted for Ptc in Glast^{+} astrocytes exhibited increased fatty acid oxidation. (A) Mean food intake reported in lean body weight (BW) during the day, night, and summed in the YFP-Ptc$^{+/+}$ and YFP-Ptc$^{-/-}$ mice 13 weeks after tamoxifen. (B) Energy expenditure normalized per BW. (C) Locomotor activity expressed as 24 h representative profile. (D and E) Respiratory exchange ratio (RER) 24 h profile (D) and representative bar graph showing the mean during the day and night (E). (F and G) Fatty acid oxidation 24 h profile (F) and representative bar graph of the mean during day and night (G). Data are represented as mean ± SEM. n = 6 mice/group, $^{*}p < 0.05$, $^{**}p < 0.01$, and $^{***}p < 0.001$.

3.6. Ptc deficiency in Glast^{+} astrocytes prevented high-fat diet-induced obesity and insulin resistance

As Ptc deficiency in Glast^{+} astrocytes reduces adiposity, improves glucose tolerance, and prevents age-associated insulin resistance, we investigated the impact of Ptc deletion on HFD-induced metabolic dysfunctions. To examine this issue, we challenged 11 weeks post—Tx YFP-Ptc$^{+/+}$ and YFP-Ptc$^{-/-}$ mice with a high-fat diet (HFD) for 12 weeks (Figure 5A). Beginning at the second week, the YFP-Ptc$^{+/+}$ mice gained more weight than the YFP-Ptc$^{-/-}$ mice that displayed full protection against HFD-induced body weight gain (Figure 5B—C and Figure Sup. 6C). At the end of the HFD challenge, SAT, VAT, and BAT of the YFP-Ptc$^{-/-}$ mice were markedly reduced, whereas the weights of the kidneys, heart, spleen, and liver were not affected (Figure 5E). Ptc deletion in astrocytes significantly reduced hepatic steatosis in the HFD-fed mice compared to the YFP-Ptc$^{+/+}$ mice (Figure 5D). Astrocytic Ptc deletion also prevented HFD-induced

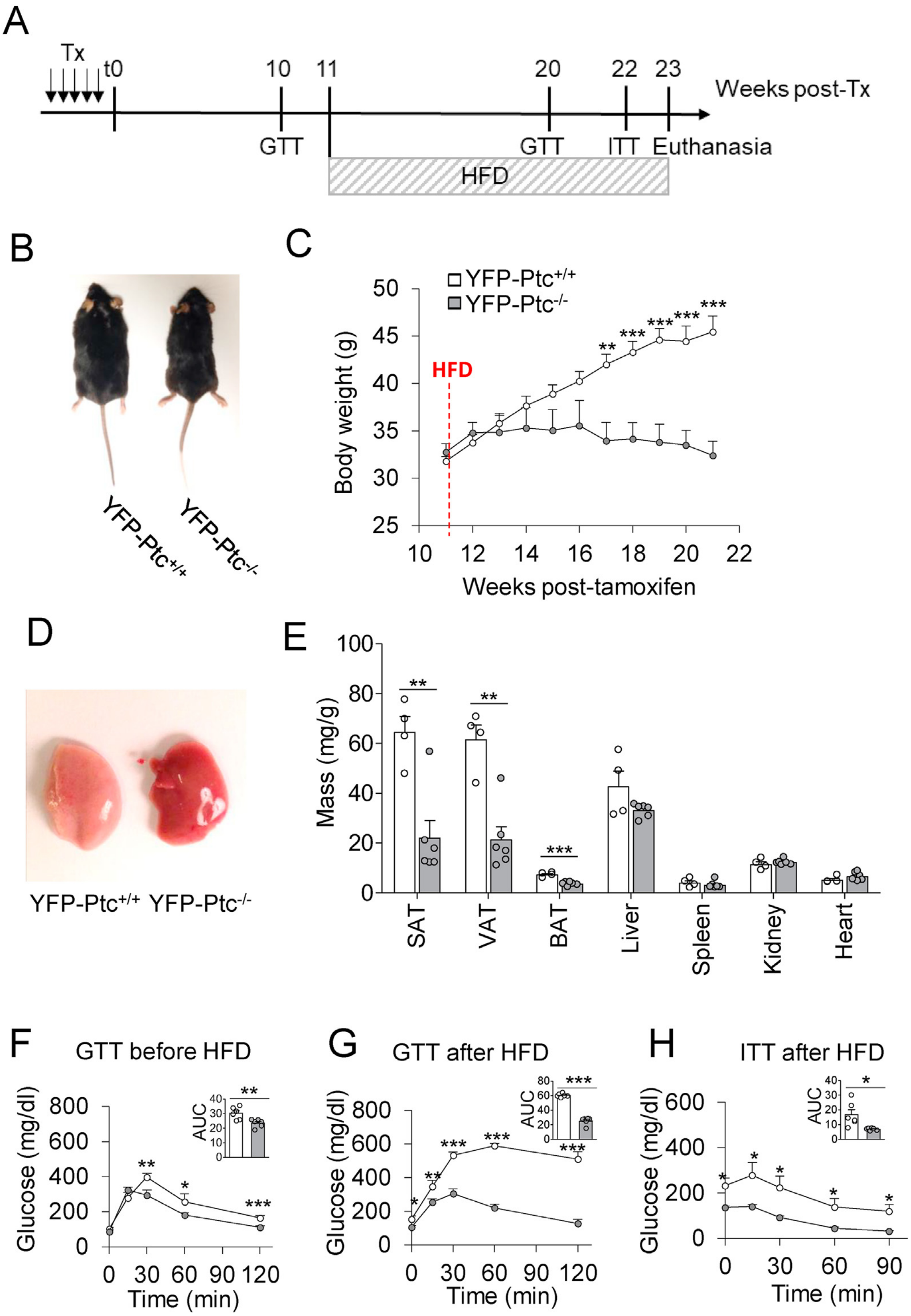

Figure 5: Ptc deletion in Glast$^+$ cells prevented HFD-induced obesity and alteration of glucose response. (A) Diagram representing the course of the experiments: high-fat diet (HFD) was started 11 weeks after the end of tamoxifen treatment (Tx) and lasted for 12 weeks. Glucose-tolerance tests (GTTs) were performed 10 and 20 weeks after Tx and insulin-tolerance tests (ITTs) 22 weeks after Tx. The mice were euthanized and tissue samples taken 23 weeks after Tx. (B) Representative images of the YFP-Ptc$^{+/+}$ and YFP-Ptc$^{-/-}$ mice after 12 weeks of the HFD. (C) Time course of body weights. Data are represented as mean ± SEM. n = 8–11 mice/group. $^{**}p < 0.01$ and $^{***}p < 0.001$ by Student's t test. (D–E) Dissected livers (D) and ratio of total organ to body weights (E) at the end of the HFD challenge. Masses of SAT, VAT, and BAT were reduced in the YFP-Ptc$^{-/-}$ mice, whereas the liver, spleen, kidney, and heart mass did not differ significantly between the two cohorts. Data are represented as mean ± SEM from n = 4–6 mice/group. $^{**}p < 0.01$ and $^{***}p < 0.001$ by Student's t test. (F–H) Blood glucose levels measured during glucose- (F and G) and (H) insulin-tolerance tests on the fasted YFP-Ptc$^{+/+}$ and YFP-Ptc$^{-/-}$ mice. Insets represent the area under the curve (AUC) of the associated graphs. Data are represented as mean ± SEM. n = 6 mice/group, $^*p < 0.05$, $^{**}p < 0.01$, and $^{***}p < 0.001$ by Student's t test. GTT, glucose-tolerance test; ITT, insulin-tolerance test; SAT, subcutaneous adipose tissue; VAT, visceral adipose tissue; BAT, brown adipose tissue.

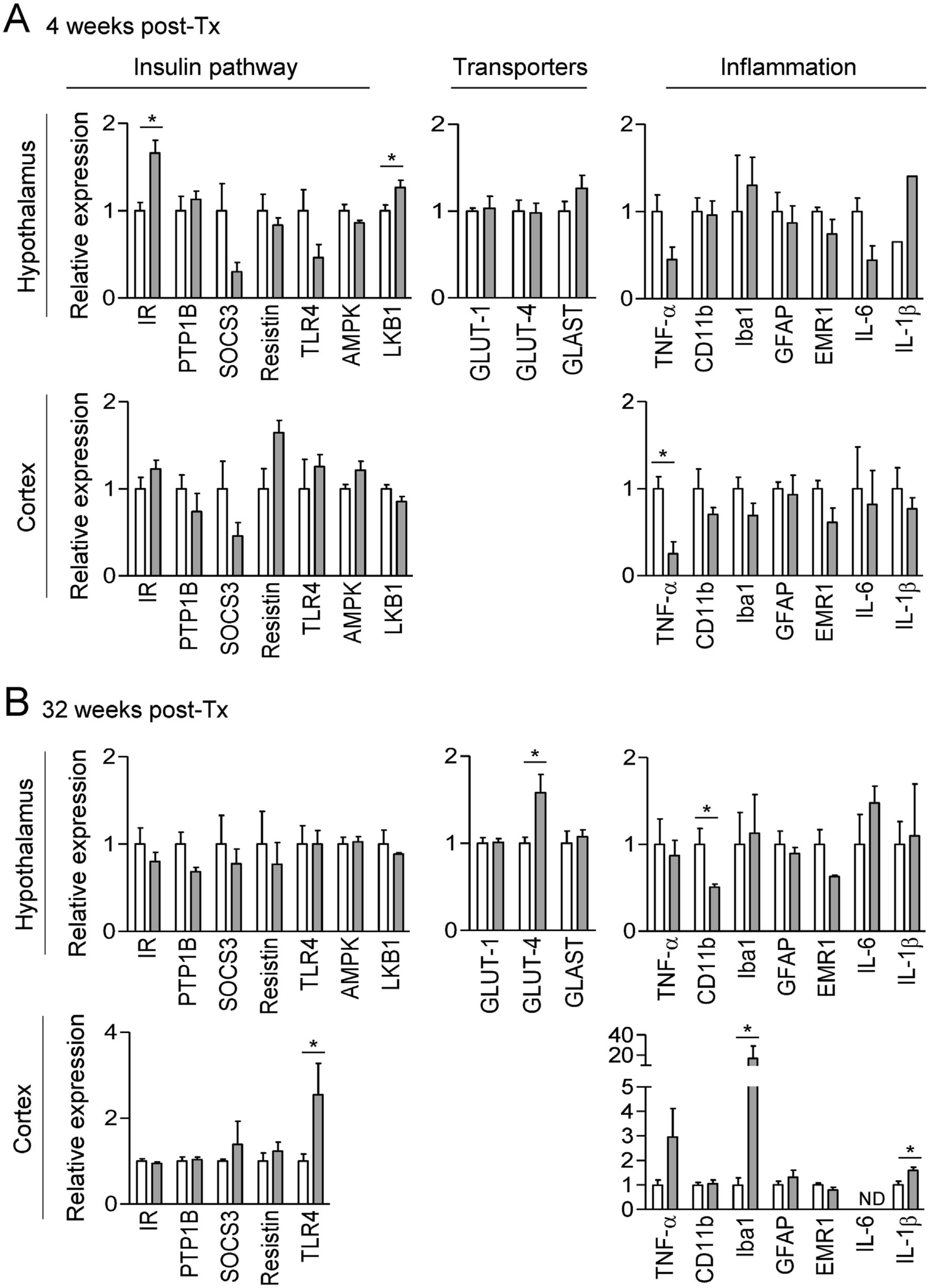

Figure 6: Effect of Ptc deletion in Glast$^+$ cells on the expression of genes implicated in insulin response, inflammation, and transport. mRNA transcripts levels of genes involved in the regulation of the insulin pathway, glucose and glutamate transport, and inflammation measured by qRT-PCR in the hypothalamus and cerebral cortex of the YFP-Ptc$^{+/+}$ and YFP-Ptc$^{-/-}$ mice 4 weeks (A) and 32 weeks (B) after tamoxifen. Actin was used as a housekeeping gene for relative mRNA expression levels. Bar graphs represent mean ± SEM. $n = 3$–4 mice/group, $^*p < 0.05$ by the Mann–Whitney test.

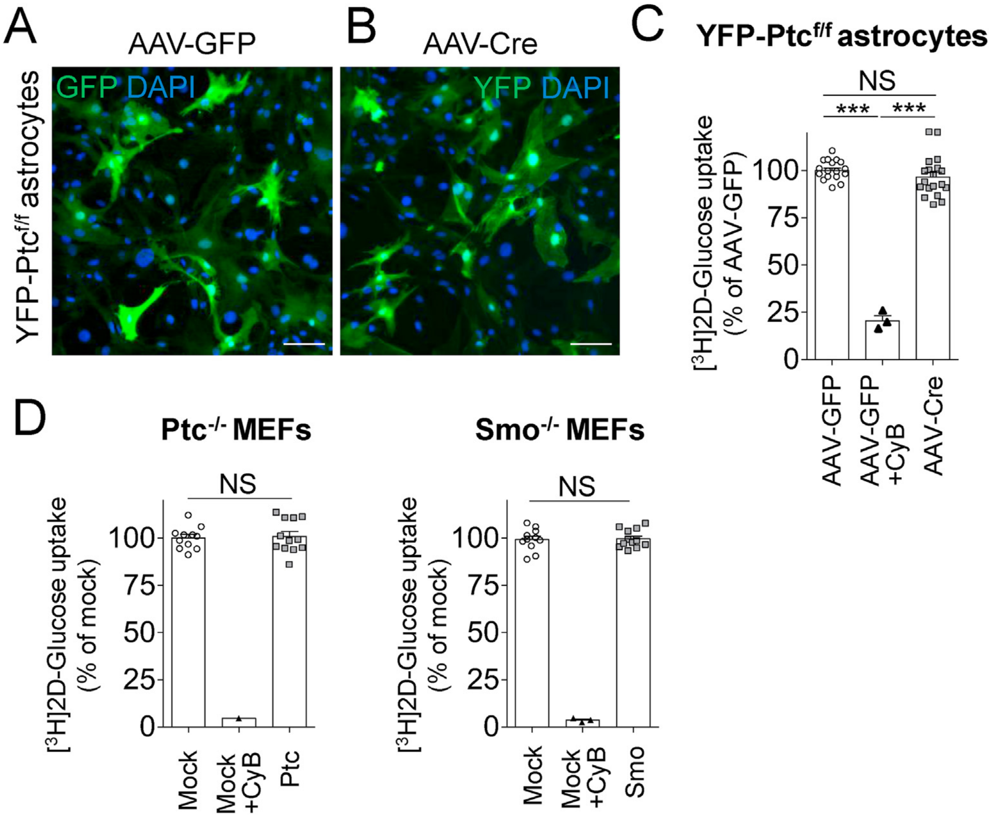

Figure 7: Glucose uptake was not affected in hypothalamic astrocytes and mouse embryonic fibroblasts upon Ptc deletion in vitro. (A—B) Primary cultures of hypothalamic astrocytes from the YFP-Ptc$^{f/f}$ mice were infected with AAV-GFP (A) as a control or AAV-Cre (B) to induce YFP expression and Ptc deletion upon recombination (see Fig. Sup. 7). Five days post-infection, cells expressed GFP or YFP as detected by immunofluorescence with a GFP antibody. (C) Cytochalasin B (10 μM) inhibited (79.5%) glucose uptake in cultured astrocytes infected with AAV-GFP as assessed using a 15 min [^{3}H]-2-deoxy-D-glucose (^{3}H-DG) uptake assay. No difference in ^{3}H-DG glucose uptake was observed in astrocytes infected with AAV-Cre compared to astrocytes infected with AAV-GFP, indicating that Ptc deletion did not significantly affect the endogenous tone of glucose uptake in these cells. Data are from three infections on three different cultures ($n = 17$, AAV-GFP; $n = 19$, AAV-Cre; $n = 3$, cytochalasin B). (D) Ptc$^{-/-}$ and Smo$^{-/-}$ MEFs were subjected to ^{3}H-DG glucose uptake after transfection with an empty control vector (Mock) or a vector for Ptc (Ptc$^{-/-}$ MEF) or Smo (Smo$^{-/-}$ MEF) expression, respectively, for rescue (see Figure Sup. 7C-D). Analysis of ^{3}H-DG uptake assay (15 min) measured 48 h after transfection indicated no difference between mocked or rescued cells ($n = 10$—12), whereas cytochalasin B (10 μM) inhibited more than 95% of ^{3}H-DG uptake in mocked cells ($n = 3$). These data suggested that both Ptc and Smo did not modify the baseline of glucose uptake in these cells. Scale bars, 100 μm. Bar graphs represent mean ± SEM. ***$p < 0.001$ by Student's t test. NS, no significant change.

hyperglycemia and glucose intolerance compared to the YFP-Ptc$^{+/+}$ mice, which exhibited higher blood glucose levels before and during the GTTs (Figure 5F—G). During the ITTs, blood glucose levels decreased 30—90 min after insulin injection in both the YFP-Ptc$^{+/+}$ and YFP-Ptc$^{-/-}$ mice but the YFP-Ptc$^{+/+}$ mice displayed higher blood glucose levels throughout the ITTs (Figure 5H). We also reported that the YFP-Ptc$^{-/-}$ mice fed a HFD displayed lower insulin and leptin blood levels compared to the YFP-Ptc$^{+/+}$ mice, whereas adiponectin levels were not affected (Table 1). Altogether, our data demonstrated that genetic activation of Shh signaling in astrocytes prevented HFD-induced obesity, glucose intolerance, and insulin resistance.

3.7. Molecular analysis upon Ptc deficiency in Glast$^+$ astrocytes indicated modifications of gene expression involved in insulin signaling in the hypothalamus

We then analyzed the expression levels of key genes involved in glucose transport, energy homeostasis, insulin sensitivity, and inflammation by qRT-PCR in hypothalamic and cerebrocortical extracts from the YFP-Ptc$^{+/+}$ and YFP-Ptc$^{-/-}$ mice after Tx (Figure 6A—B). Four weeks after Tx, we observed from the hypothalamic extracts a significant upregulation of the mRNA expression of insulin receptor (IR) and LKB1 and a downregulation of the mRNA levels of TLR4 and the negative regulator of the insulin pathway SOCS3, albeit it did not reach significance (Figure 6A). These modifications were not exhibited in the mutant animals 32 weeks after Tx (Figure 6B). We did not observe these changes in the cerebral cortex of these animals at either 4 or 32 weeks post—Tx (Figure 6A—B). In hypothalamic extracts, the mRNA expression of glucose transporter GLUT-4 was upregulated in the mutant mice 32 weeks but not 4 weeks post—Tx, whereas GLUT-1 and Glast were not modified over time (Figure 6A—B). The increase in fatty acid oxidation (Figure 4F—G) and the marked decrease in adipose tissue depots (Figure 3C—E) observed in the YFP-Ptc$^{-/-}$ mice were accompanied by decreased gene expression of the proinflammatory cytokines TNFα and IL6 in the hypothalamus 4 weeks after Tx, whereas a significant decrease in hypothalamic CD11b was observed 32 weeks after Tx (Figure 6A—B). However, most of the other inflammatory pathway genes, including GFAP, were not affected (Figure 6A—B). Interestingly, inflammatory-related gene levels were also modified in the cortex following Ptc deletion in Glast$^+$ astrocytes. The TNF-α mRNA level was significantly decreased in the YFP-Ptc$^{-/-}$ mice 4 weeks after Tx while the aged YFP-Ptc$^{-/-}$ mice (32 weeks after Tx) displayed an increased expression of TNF-α, Iba1, and IL-1β (Figure 6A—B).

3.8. Ablation of patched in Glast-positive cells did not modify glucose availability in astrocytes

We then investigated the effect of Ptc deletion in Glast$^+$ cells on glucose availability in primary hypothalamic astrocyte cultures from the YFP-Ptc$^{fl/fl}$ pups on post-natal day 1. These cultures were infected with an adenovirus for Cre delivery for recombination or an adenovirus for GFP expression. First, we demonstrated that the adenoviral delivery of GFP or Cre led to a wide expression of GFP and YFP in astrocyte cultures, respectively (Figure 7A—B), and the deletion of the floxed region of Ptc mRNA as evidenced by the qRT-PCR analysis (Figure Sup. 7A). The loss of the Ptc receptor had no effect on [^{3}H]-2-deoxy-D-glucose (^{3}H-DG) uptake during a 15 min-assay in these cells, whereas treatment with cytochalasin B, an inhibitor of glucose transporters [32], blocked ~80% of ^{3}H-DG uptake (Figure 7C). We then investigated whether ^{3}H-DG uptake in Ptc$^{-/-}$ MEFs and Smo$^{-/-}$ MEFs was modified upon rescue with Ptc and Smo overexpressing vectors, respectively. We observed a robust expression of both Ptc and Smo transcripts upon overexpression of Ptc and Smo vectors, respectively, and upregulation of the Hh pathway in Ptc$^{-/-}$ MEF cells indicated by high *Gli1* transcription as expected (Figure Sup. 7B—D). However, we did not detect modification of ^{3}H-DG uptake in these cells upon rescue with Ptc or Smo, whereas cytochalasin B efficiently inhibited ^{3}H-DG uptake by ~95% (Figure 7D). Altogether, these data indicate that ablation of Ptc in primary astrocyte cultures or Ptc and Smo in MEFs did not affect the endogenous tone of glucose uptake in these cells.

4. DISCUSSION

In this report, we provide in vivo evidence that astrocytic Shh signaling in the brain exerts a key role in the control of energy metabolism. We demonstrated that genetic activation of Shh signaling in Glast-positive astrocytes in the adult brain resulted in a lean phenotype associated with an increase in fatty acid oxidation and full protection against age- or nutrient-induced metabolic defects. In our model, Ptc deficiency in Glast-positive astrocytes enhanced insulin sensitivity and improved glucose tolerance, resulting in an increase in blood glucose uptake and a decrease in blood insulin levels, with a pronounced resistance to age-associated and diet-induced metabolic alterations. Expression of genes associated with Shh and insulin signaling was modified in hypothalamic tissues from the mutant animals, whereas astrocyte glucose availability was not altered in primary hypothalamic astrocyte cultures upon Ptc deletion. Altogether, these data indicate hypothalamic control of energy metabolism through Shh signaling regulation in astrocytes.

To achieve selective activation of Shh signaling in astrocytes, we used a time-controlled Cre driver regulated by the Glast promoter widely used for specific expression of transgenes in astrocytes [7,17,33,34]. First, we identified selective expression of the YFP reporter in GFAP-positive hypothalamic astrocytes but not in cells expressing the neuronal marker HuC/D or oligodendroglial marker NG2. We then demonstrated that *Ptc* expression occurred in 87—94% of hypothalamic astrocytes expressing S100β and *Glast*. Single cell analysis of the *Ptc* expression in YFP-Ptc$^{+/+}$ and YFP-Ptc$^{-/-}$ mouse brain sections by RNAscope showed that nearly all of the hypothalamic astrocytes underwent Cre-mediated recombination, which was further supported by RT-PCR analysis of hypothalamic extracts showing a decrease in Ptc mRNA and an increase in Ptc^{del} transcripts in the YFP-Ptc$^{-/-}$ mice.

The effects of Ptc deficiency were relatively strong. The lean phenotype of the YFP-Ptc$^{-/-}$ mice also observed upon the HFD was accompanied by a marked decrease in both white and brown adipose tissues, improved glucose tolerance, and reduced insulin levels. This might reflect the high level of Ptc inactivation in hypothalamic Glast$^+$ astrocytes observed in our experiments and the important role of astrocytes in regulating these parameters [18]. Interestingly, the increase in glucose tolerance was already observed 5 days post—Tx, suggesting the rapid consequences of central Ptc inactivation on overall glucose homeostasis.

We identified a non-uniform distribution of Ptc, Gli1, Gli2, and Gli3 in adult mouse hypothalamic nuclei, suggesting that complex canonical and non-canonical Shh signaling occurred in this region: i) Gli1-Gli3 were almost exclusively expressed in astrocytes, whereas Ptc was also present in neurons, in agreement with our previous work [9] and ii) Gli1-Gli3 were highly expressed in most hypothalamic astrocytes (80—97%), except in the ARC, where Gli2 and Gli3 expression was lower (63—72%).

Canonical Shh signaling associated with Gli1 transcription occurred in hypothalamic and cerebrocortical astrocytes upon Ptc deletion as evidenced by qRT-PCR of brain extracts and quantitative RNAscope analysis. We also observed an opposite effect of Shh signaling activation on Gli3 regulation in ARC and DMH astrocytes compared to cerebrocortical astrocytes: the population of Gli3$^+$ astrocytes increased in the ARC and DMH, whereas it decreased in the cerebrocortical region. Interestingly, the lack of Gli3 transcript expression change in the VMH may underscore heterogeneity in hypothalamic astrocytes.

In the cortex, the increased number of Gli1$^+$ and decreased number of Gli3$^+$ astrocytes may have been associated with the downregulation of the repressive form of Gli3 (Gli3^R), antagonist of the Shh pathway, and an increase of Gli1 transcription. Indeed, Gli3^R has been proposed to play a dominant role in regulating Shh signaling in mature cerebrocortical astrocytes and mediate astrocyte gliosis [35]. Further investigations should address whether the increased level of Gli3 transcripts in ARC and DMH reflects an increase in Gli3^R or the activated forms of Gli3 (Gli3^A) that have been described in embryos [36,37]. Thus, in addition to canonical Shh signaling [3,20,35], other non-canonical Gli-dependent and independent mechanisms may exist in hypothalamic astrocytes [2,13].

Ptc deletion in Glast$^+$ astrocytes in the adult brain has been associated with an upregulation in the cortex of the inward-rectifying K$^+$ channel Kir4.1 involved in glutamate uptake [38]. Interestingly, we did not detect modifications of gene expression levels of the astrocyte-specific glutamate transporter Glast or glucose transporters GLUT-1 and GLUT-4 in the YFP-Ptc$^{-/-}$ animals four weeks post—Tx. However, the GLUT-4 level was significantly upregulated 32 weeks post—Tx, suggesting that glucose transport might have been affected in the brains of the aged mutant animals through still unknown mechanisms.

Age-related increase in the plasma insulin level is a classic feature of age-related deterioration of insulin sensitivity in rodents. Insulinemia remained low and in the same range over time in the YFP-Ptc$^{-/-}$ mice, suggesting that astrocytic Shh signaling is a core component relaying metabolic alterations associated with aging. Further experiments are needed to investigate the impact of astrocytic Ptc deletion on pancreatic insulin secretion, peripheral insulin signaling and sensitivity, and whether insulin-independent mechanisms of glucose regulation already described [18,39,40] could also have been involved in the YFP-Ptc$^{-/-}$ mice. Our data also demonstrated an improvement in overall glucose tolerance in both the young and aged YFP-Ptc$^{-/-}$ mice, an effect also observed upon challenge with the HFD. However, the GTT response curves may have been exacerbated in the aged YFP-Ptc$^{-/-}$ mice under regular chow or with the HFD since they displayed a pronounced lean phenotype and thus received less glucose. Indeed, Ptc deletion in astrocytes prevented the development of insulin resistance observed in the aged animals or resulting from diet-induced obesity.

The body weights of the control and mutant animals were not significantly different six weeks after Tx despite a tighter control of blood glucose availability in the YFP-Ptc$^{-/-}$ mice. The lean phenotype observed in the mutant mice was associated with profound alterations of adipose tissue metabolism, including SAT, VAT, and BAT, the size of adipocytes being considerably reduced upon Ptc deletion. The lean phenotype was also associated with changes in fatty acid oxidation that increased during the day and decreased at night. Ptc deletion on astrocytes had no effect on body temperature, food intake, and energy expenditure, suggesting that the circuitry implicated in these complexes behaviors were not affected [18,41].

The mice lacking the Ptc receptor in astrocytes also exhibited reduced weight of SAT, VAT, and BAT in response to the HFD. Moreover, astrocytic Ptc deficiency prevented HFD-induced hepatic steatosis, which is a hallmark of an exacerbated response to a HFD. Thus, these data suggested that genetic activation of Shh signaling in Glast^{+} cells prevented features encountered in obesity such as excessive accumulation of adipose tissues, insulin resistance, and liver steatosis.

Genetic variants of human Ptc with loss-of-function mutations are associated with medulloblastoma, a pediatric brain tumor with devastating effects [13]. Mice with mutations in Ptc are proposed as models of medulloblastoma [42,43]. However, whether these mutations are associated with impaired energy metabolism and body weight in humans or rodents has not been reported to the best of our knowledge. In Ptc$^{mes/mes}$, deletion of the carboxyl-terminal region of Ptc is accompanied by reduced white fat mass, whereas glucose levels are not affected [44]. This suggests that the truncated Ptc region is not involved in mediating Ptc effects in the control of blood glucose homeostasis by hypothalamic astrocytes in our experiments. It would be of interest to investigate if human-inactivating Ptc alleles contribute to a lean phenotype in individuals with or without additional genetic predisposition to obesity.

Further studies are warranted to delineate the transduction mechanisms involved in mediating astrocytic Ptc effects on the control of energy metabolism and if small molecule modulators of Smo are of interest in their modulation. Smo antagonists are used in clinics to treat medulloblastoma and basal cell carcinoma associated with dysfunction of Hh signaling [1]. Interestingly, one of these molecules, GDC0449, has been proposed to act as a non-canonical Smo agonist driving insulin-independent glucose uptake mediated by AMPK in muscle and brown adipose tissues [15], highlighting the complex transduction mechanisms associated with Hh signaling in tissues. Other canonical or non-canonical Smo agonists [13,45] are not yet in clinics but might be of interest for dissecting the in vitro and in vivo biochemical and molecular events associated with Shh signaling in astrocytes. Ptc deletion in primary cultures of astrocytes did not modify glucose uptake, and biochemical experiments using Ptc$^{-/-}$ MEFs and Smo$^{-/-}$ MEFs did not support the hypothesis that Ptc mediates glucose uptake in these cells. Thus, astrocytes do not share the non-canonical AMPK axis implicated in glucose uptake in muscle and adipose tissues [15] and the metabolic effects of astrocytic Ptc deletion do not seem to be mediated by modification of astrocyte glucose uptake.

Hh signaling in adipose tissue development and as a potent inhibitor of fat formation has been documented in both rodents and *Drosophila*, whereas the modulation by the adiposity pathway in these tissues in the adult stage is still poorly understood [46—49]. Herein, we report another level of regulation of adipose tissue physiology in the adult mice induced by the alteration of astrocytic Hh signaling.

What are the likely mechanisms mediating the remarkable metabolic effects of astrocyte-specific ablation of Ptc in our model? Hypothalamic nuclei including the ARC, VMH, and DMH are involved in the control of systemic glucose homeostasis through the complex regulation of multiple hypothalamic circuits involving neuronal and astrocytic populations [39]. One hypothesis to explain the observed effects is that the genetic manipulation of Shh signaling in astrocytes modifies the release of endogenous molecules that participate in the central control of energy homeostasis. Part of this regulation may also involve parasympathetic nervous activities since the autonomic nervous system controls key events mediated by peripheral tissues implicated in metabolic activities such as the liver, muscle, or fat but also pancreatic hormone secretion [18,41]. The lean phenotype is plausibly driven by a net increase in whole-body β oxidation observed during the day, with no change in food intake, body temperature, or total energy expenditure. This phenotype may involve the induction of AMPK, possibly through LKB1 phosphorylation, a response to fasting or nutritional deficit generally accompanied by increased whole-body β oxidation, presumably in response to hypothalamic signals [18,50—52]. Although glucose uptake was not altered in our model, induction of AMPK may have shifted the astrocytes to β oxidation, so glucose metabolism was reduced. This effect would reduce glucose signaling to hypothalamic neurons, thus producing whole-body β oxidation and reduce adiposity [53—55].

5. CONCLUSIONS

Shh signaling is present in mouse hypothalamic astrocytes. Conditional genetic activation of the pathway in Glast^{+} astrocytes results in an increased sensitivity to blood glucose levels and lower blood insulin. Strikingly, the strong lean phenotype observed in the mutant animals was associated with a blockade of weight gain with a profound reduction in white and brown adipose tissues and an increase in fatty acid oxidation. Thus, Shh signaling in astrocytes appears to have a central role in counteracting metabolic defects observed during aging and obesity. This study reveals how hypothalamic astrocytes significantly impact the physiology and pathophysiology through Shh signaling in adults and may provide a novel target for potential anti-obesity strategies.

AUTHOR CONTRIBUTIONS

L.T., M.R., G.P., H.F., C.D., M.D. and A.S. were responsible for data collection, analysis, and interpretation. M.R. was responsible for the conception and study design, data collection, interpretation, and drafting. Y.B., M.T., J.A., S.L., R.D., and S.L. were involved in the design, data collection, analysis, and interpretation. Critical revision of the article and final approval was confirmed by all of the authors.

DATA ACCESSIBILITY STATEMENT

Contact the corresponding author for primary data material assessment.

CONFLICTS OF INTEREST

The authors have no competing interests to declare.

ACKNOWLEDGMENTS

M.R. and L.T. are recipients of a doctoral fellowship from the Ministère de la Recherche and L.T. from Fondation pour l'Aide à la Recherche sur la Sclérose En

Plaque (ARSEP), respectively. This study was supported by grants from ARSEP, Association pour la Recherche contre le Cancer (ARC), and CNRS to M.R. We acknowledge the technical platform Functional and Physiological Exploration platform (FPE) of the Université de Paris, BFA, UMR 8251, CNRS, Paris, France, and the animal core facility of the Institut Jacques Monod.

ABBREVIATIONS

3V	third ventricle
βgal	βgalactosidase
Cb	cerebellum
cc	corpus callosum
CNS	central nervous system
Ctx	cortex
DG	dentate gyrus
Ep	ependymal layer
GFAP	glial fibrillary acidic protein
GST	glutathione-S-transferase
HEK	human embryonic kidney
Hpt	hypothalamus
Iba1	ionized calcium-binding adapter molecule 1
ME	median eminence
Olig2	oligodendrocyte transcription factor 2
Ptc	Patched
Shh	Sonic Hedgehog
ShhN	amino-terminal fragment of Shh
Sox10	SRY-Box 10

APPENDIX A. SUPPLEMENTARY DATA

Supplementary data to this article can be found online at https://doi.org/10.1016/j.molmet.2021.101172.

REFERENCES

[1] Ruat, M., Faure, H., Daynac, M., 2015. Smoothened, stem cell maintenance and brain diseases. Topics in Medicinal Chemistry 16:147—171.

[2] Garcia, A.D.R., Han, Y.G., Triplett, J.W., Farmer, W.T., Harwell, C.C., Ihrie, R.A., 2018. The elegance of Sonic hedgehog: emerging novel functions for a classic morphogen. Journal of Neuroscience 38(44):9338—9345.

[3] Garcia, A.D., Petrova, R., Eng, L., Joyner, A.L., 2010. Sonic hedgehog regulates discrete populations of astrocytes in the adult mouse forebrain. Journal of Neuroscience 30(41):13597—13608.

[4] Allahyari, R.V., Clark, K.L., Shepard, K.A., Garcia, A.D.R., 2019. Sonic hedgehog signaling is negatively regulated in reactive astrocytes after forebrain stab injury. Scientific Reports 9(1):565.

[5] Pascual, O., Traiffort, E., Baker, D.P., Galdes, A., Ruat, M., Champagnat, J., 2005. Sonic hedgehog signalling in neurons of adult ventrolateral nucleus tractus solitarius. European Journal of Neuroscience 22(2):389—396.

[6] Bezard, E., Baufreton, J., Owens, G., Crossman, A.R., Dudek, H., Taupignon, A., et al., 2003. Sonic hedgehog is a neuromodulator in the adult subthalamic nucleus. The FASEB Journal 17(15):2337—2338.

[7] Farmer, W.T., Abrahamsson, T., Chierzi, S., Lui, C., Zaelzer, C., Jones, E.V., et al., 2016. Neurons diversify astrocytes in the adult brain through sonic hedgehog signaling. Science 351(6275):849—854.

[8] Liu, Y., Yuelling, L.W., Wang, Y., Du, F., Gordon, R.E., O'Brien, J.A., et al., 2017. Astrocytes promote medulloblastoma progression through hedgehog secretion. Cancer Research 77(23):6692—6703.

[9] Tirou, L., Russo, M., Faure, H., Pellegrino, G., Sharif, A., Ruat, M., 2020. C9C5 positive mature oligodendrocytes are a source of Sonic Hedgehog in the mouse brain. PLoS One 15(2):e0229362.

[10] Gonzalez-Reyes, L.E., Verbitsky, M., Blesa, J., Jackson-Lewis, V., Paredes, D., Tillack, K., et al., 2012. Sonic hedgehog maintains cellular and neurochemical homeostasis in the adult nigrostriatal circuit. Neuron 75(2):306—319.

[11] Ferent, J., Zimmer, C., Durbec, P., Ruat, M., Traiffort, E., 2013. Sonic hedgehog signaling is a positive oligodendrocyte regulator during demyelination. Journal of Neuroscience 33(5):1759—1772.

[12] Samanta, J., Grund, E.M., Silva, H.M., Lafaille, J.J., Fishell, G., Salzer, J.L., 2015. Inhibition of Gli1 mobilizes endogenous neural stem cells for remyelination. Nature 526(7573):448—452.

[13] Ruat, M., Hoch, L., Faure, H., Rognan, D., 2014. Targeting of Smoothened for therapeutic gain. Trends in Pharmacological Sciences 35(5):237—246.

[14] Kong, J.H., Siebold, C., Rohatgi, R., 2019. Biochemical mechanisms of vertebrate hedgehog signaling. Development 146(10).

[15] Teperino, R., Amann, S., Bayer, M., McGee, S.L., Loipetzberger, A., Connor, T., et al., 2012. Hedgehog partial agonism drives warburg-like metabolism in muscle and Brown fat. Cell 151(2):414—426.

[16] Fleury, A., Hoch, L., Martinez, M.C., Faure, H., Taddei, M., Petricci, E., et al., 2016. Hedgehog associated to microparticles inhibits adipocyte differentiation via a non-canonical pathway. Scientific Reports 6:23479.

[17] Garcia-Caceres, C., Quarta, C., Varela, L., Gao, Y., Gruber, T., Legutko, B., et al., 2016. Astrocytic insulin signaling couples brain glucose uptake with nutrient availability. Cell 166(4):867—880.

[18] Garcia-Caceres, C., Balland, E., Prevot, V., Luquet, S., Woods, S.C., Koch, M., et al., 2019. Role of astrocytes, microglia, and tanycytes in brain control of systemic metabolism. Nature Neuroscience 22(1):7—14.

[19] Dallerac, G., Zapata, J., Rouach, N., 2018. Versatile control of synaptic circuits by astrocytes: where, when and how? Nature Reviews Neuroscience 19(12): 729—743.

[20] Traiffort, E., Charytoniuk, D., Watroba, L., Faure, H., Sales, N., Ruat, M., 1999. Discrete localizations of hedgehog signalling compotents in the developing and adult rat nervous system. European Journal of Neuroscience 11:3199—3214.

[21] Coulombe, J., Traiffort, E., Loulier, K., Faure, H., Ruat, M., 2004. Hedgehog interacting protein in the mature brain: membrane-associated and soluble forms. Molecular and Cellular Neuroscience 25(2):323—333.

[22] Ferent, J., Cochard, L., Faure, H., Taddei, M., Hahn, H., Ruat, M., et al., 2014. Genetic activation of hedgehog signaling unbalances the rate of neural stem cell renewal by increasing symmetric divisions. Stem Cell Reports 3(2):312—323.

[23] Masdeu, C., Faure, H., Coulombe, J., Schoenfelder, A., Mann, A., Brabet, I., et al., 2006. Identification and characterization of Hedgehog modulator properties after functional coupling of Smoothened to G15. Biochemical and Biophysical Research Communications 349(2):471—479.

[24] Traiffort, E., Moya, K.L., Faure, H., Hassig, R., Ruat, M., 2001. High expression and anterograde axonal transport of aminoterminal sonic hedgehog in the adult hamster brain. European Journal of Neuroscience 14(5):839—850.

[25] Peterfi, Z., Farkas, I., Denis, R.G.P., Farkas, E., Uchigashima, M., Fuzesi, T., et al., 2018. Endocannabinoid and nitric oxide systems of the hypothalamic paraventricular nucleus mediate effects of NPY on energy expenditure. Molecular Genetics and Metabolism 18:120—133.

[26] Poizat, G., Alexandre, C., Al Rifai, S., Riffault, L., Crepin, D., Benomar, Y., et al., 2019. Maternal resistin predisposes offspring to hypothalamic inflammation and body weight gain. PLoS One 14(3):e0213267.

[27] Zibat, A., Uhmann, A., Nitzki, F., Wijgerde, M., Frommhold, A., Heller, T., et al., 2009. Time-point and dosage of gene inactivation determine the tumor spectrum in conditional Ptch knockouts. Carcinogenesis 30(6):918—926.

[28] Angot, E., Loulier, K., Nguyen-Ba-Charvet, K.T., Gadeau, A.P., Ruat, M., Traiffort, E., 2008. Chemoattractive activity of sonic hedgehog in the adult subventricular zone modulates the number of neural precursors reaching the olfactory bulb. Stem Cells 26(9):2311—2320.

[29] Andreu-Cervera, A., Anselme, I., Karam, A., Laclef, C., Catala, M., Schneider-Maunoury, S., 2019. The ciliopathy gene Ftm/Rpgrip1l controls mouse

forebrain patterning via region-specific modulation of Hedgehog/Gli signaling. Journal of Neuroscience 39(13):2398—2415.

[30] Rivell, A., Petralia, R.S., Wang, Y.X., Clawson, E., Moehl, K., Mattson, M.P., et al., 2019. Sonic hedgehog expression in the postnatal brain. The Open Biology Journal 8(3).

[31] Daynac, M., Tirou, L., Faure, H., Mouthon, M.A., Gauthier, L.R., Hahn, H., et al., 2016. Hedgehog controls quiescence and activation of neural stem cells in the adult ventricular-subventricular zone. Stem Cell Reports 7(4):735—748.

[32] Augustin, R., 2010. The protein family of glucose transport facilitators: it's not only about glucose after all. IUBMB Life 62(5):315—333.

[33] Barca-Mayo, O., Pons-Espinal, M., Follert, P., Armirotti, A., Berdondini, L., De Pietri Tonelli, D., 2017. Astrocyte deletion of Bmal1 alters daily locomotor activity and cognitive functions via GABA signalling. Nature Communications 8: 14336.

[34] Zhang, N., Zhang, Z., He, R., Li, H., Ding, S., 2020. GLAST-CreER(T2) mediated deletion of GDNF increases brain damage and exacerbates long-term stroke outcomes after focal ischemic stroke in mouse model. Glia 68(11):2395—2414.

[35] Petrova, R., Garcia, A.D., Joyner, A.L., 2013. Titration of GLI3 repressor activity by sonic hedgehog signaling is critical for maintaining multiple adult neural stem cell and astrocyte functions. Journal of Neuroscience 33(44):17490—17505.

[36] Bai, C.B., Stephen, D., Joyner, A.L., 2004. All mouse ventral spinal cord patterning by hedgehog is Gli dependent and involves an activator function of Gli3. Developmental Cell 6(1):103—115.

[37] Bowers, M., Eng, L., Lao, Z., Turnbull, R.K., Bao, X., Riedel, E., et al., 2012. Limb anterior-posterior polarity integrates activator and repressor functions of GLI2 as well as GLI3. Developmental Biology 370(1):110—124.

[38] Hill, S.A., Blaeser, A.S., Coley, A.A., Xie, Y., Shepard, K.A., Harwell, C.C., et al., 2019. Sonic hedgehog signaling in astrocytes mediates cell-type-specific synaptic organization. Elife 8.

[39] Ruud, J., Steculorum, S.M., Bruning, J.C., 2017. Neuronal control of peripheral insulin sensitivity and glucose metabolism. Nature Communications 8:15259.

[40] Brewer, P.D., Romenskaia, I., Mastick, C.C., 2019. A high-throughput chemical-genetics screen in murine adipocytes identifies insulin-regulatory pathways. Journal of Biological Chemistry 294(11):4103—4118.

[41] Timper, K., Bruning, J.C., 2017. Hypothalamic circuits regulating appetite and energy homeostasis: pathways to obesity. Disease Model Mechanisms 10(6): 679—689.

[42] Yang, Z.J., Ellis, T., Markant, S.L., Read, T.A., Kessler, J.D., Bourboulas, M., et al., 2008. Medulloblastoma can be initiated by deletion of Patched in lineage-restricted progenitors or stem cells. Cancer Cell 14(2):135—145.

[43] Goodrich, L.V., Milenkovic, L., Higgins, K.M., Scott, M.P., 1997. Altered neural cell fates and medulloblastoma in mouse patched mutants. Science 277(5329):1109—1113.

[44] Li, Z., Zhang, H., Denhard, L.A., Liu, L.H., Zhou, H., Lan, Z.J., 2008. Reduced white fat mass in adult mice bearing a truncated Patched 1. International Journal of Biological Sciences 4(1):29—36.

[45] Teperino, R., Aberger, F., Esterbauer, H., Riobo, N., Pospisilik, J.A., 2014. Canonical and non-canonical Hedgehog signalling and the control of metabolism. Seminars in Cell & Developmental Biology 33:81—92.

[46] Pospisilik, J.A., Schramek, D., Schnidar, H., Cronin, S.J., Nehme, N.T., Zhang, X., et al., 2010. Drosophila genome-wide obesity screen reveals hedgehog as a determinant of brown versus white adipose cell fate. Cell 140(1):148—160.

[47] Nosavanh, L., Yu, D.H., Jaehnig, E.J., Tong, Q., Shen, L., Chen, M.H., 2015. Cell-autonomous activation of Hedgehog signaling inhibits brown adipose tissue development. Proceedings of the National Academy of Sciences of the U S A 112(16):5069—5074.

[48] Braune, J., Weyer, U., Matz-Soja, M., Hobusch, C., Kern, M., Kunath, A., et al., 2017. Hedgehog signalling in myeloid cells impacts on body weight, adipose tissue inflammation and glucose metabolism. Diabetologia 60(5):889—899.

[49] Lee, H.J., Jo, S.B., Romer, A.I., Lim, H.J., Kim, M.J., Koo, S.H., et al., 2015. Overweight in mice and enhanced adipogenesis in vitro are associated with lack of the hedgehog coreceptor boc. Diabetes 64(6):2092—2103.

[50] Martins, L., Seoane-Collazo, P., Contreras, C., Gonzalez-Garcia, I., Martinez-Sanchez, N., Gonzalez, F., et al., 2016. A functional link between AMPK and orexin mediates the effect of BMP8B on energy balance. Cell Reports 16(8): 2231—2242.

[51] Wang, B., Cheng, K.K., 2018. Hypothalamic AMPK as a mediator of hormonal regulation of energy balance. International Journal of Molecular Sciences 19(11).

[52] Voss, C.M., Andersen, J.V., Jakobsen, E., Siamka, O., Karaca, M., Maechler, P., et al., 2020. AMP-activated protein kinase (AMPK) regulates astrocyte oxidative metabolism by balancing TCA cycle dynamics. Glia 68(9): 1824—1839.

[53] Bentsen, M.A., Mirzadeh, Z., Schwartz, M.W., 2019. Revisiting how the brain senses glucose-and why. Cell Metabolism 29(1):11—17.

[54] Hirschberg, P.R., Sarkar, P., Teegala, S.B., Routh, V.H., 2020. Ventromedial hypothalamus glucose-inhibited neurones: a role in glucose and energy homeostasis? Journal of Neuroendocrinology 32(1):e12773.

[55] Stanley, S., Moheet, A., Seaquist, E.R., 2019. Central mechanisms of glucose sensing and counterregulation in defense of hypoglycemia. Endocrine Reviews 40(3):768—788.